

ON THE NATURE OF THE COMPACT OBJECT IN SS 433: OBSERVATIONAL EVIDENCE OF X-RAY PHOTON INDEX SATURATION

ELENA SEIFINA¹ AND LEV TITARCHUK^{2,3,4}

¹ Moscow State University/Sternberg Astronomical Institute, Universitetsky Prospect 13, Moscow 119992, Russia; seif@sai.msu.ru

² Dipartimento di Fisica, Università di Ferrara, Via Saragat 1, I-44100 Ferrara, Italy; titarchuk@fe.infn.it

³ George Mason University, Fairfax, VA 22030, USA

⁴ NASA/Goddard Space Flight Center, Code 663, Greenbelt, MD 20771, USA; lev@milkyway.gsfc.nasa.gov

Received 2010 April 1; accepted 2010 August 17; published 2010 September 22

ABSTRACT

We present an analysis of the X-ray spectral properties observed from the black hole candidate (BHC) binary SS 433. We have analyzed *Rossi X-ray Timing Explorer* data from this source, coordinated with Green Bank Interferometer/RATAN-600. We show that SS 433 undergoes an X-ray spectral transition from the low hard state to the intermediate state (IS). We show that the X-ray broadband energy spectra during all spectral states are well fitted by a sum of the so-called bulk motion Comptonization (BMC) component and by two (broad and narrow) Gaussians for the continuum and line emissions, respectively. In addition to these spectral model components, we also find a strong feature that we identify as a “blackbody-like (BB)” component in which the color temperature is in the range of 4–5 keV in 24 IS spectra during the radio outburst decay in SS 433. Our observational results on the “high-temperature BB” bump lead us to suggest the presence of gravitationally redshifted annihilation line emission in this source. In fact, this spectral feature has been recently reproduced in Monte Carlo simulations by Laurent & Titarchuk. We have also established the photon index saturation at about 2.3 in index versus mass accretion correlation. This index–mass accretion correlation allows us to evaluate the low limit of the black hole (BH) mass of the compact object in SS 433, $M_{\text{bh}} \gtrsim 2$ solar masses, using the scaling method using BHC GX 339–4 as a reference source. Our estimate of the BH mass in SS 433 is consistent with the recent BH mass measurement using the radial velocity measurements of the binary system by Hillwig & Gies, who find that $M_x = (4.3 \pm 0.8)$ solar masses. This is the smallest BH mass found up to now among all BH sources. Moreover, the index saturation effect versus mass accretion rate revealed in SS 433, as in a number of other BH candidates, is strong observational evidence for the presence of a BH in SS 433.

Key words: accretion, accretion disks – black hole physics – stars: individual (SS 433)

Online-only material: color figures

1. INTRODUCTION

The famous object SS 433 (V 1343 Aql) holds a special place in late twentieth-century astronomy as the first microquasar discovered in our Galaxy (see reviews by Margon 1984 and Fabrika 2004). Observations of SS 433 have been carried out in all energy ranges for more than 30 years. Its key observational feature is the 162.5 day precession period of the jets that is revealed by the line features. The radial velocity curves of these lines are well described by a kinematical model which reveals key parameters of the jets: $v = 0.26c$ and $i = 79^\circ$ (Margon 1984). Moreover, Romney et al. (1987) used and combined these results with the radio observations of the associated supernova remnant W50 which allowed them to estimate a distance of 5 kpc to SS 433.

SS 433 is an X-ray/optical binary with Algol-type orbital eclipses. This source is characterized by two distinct spectral states: the quiescent hard state in which the persistent jet flow takes place and the soft state when massive jet blobs are ejected (Fielder et al. 1987). While the quiescent state has been well studied by numerous X-ray missions, only a few massive jet ejection events simultaneous with the X-ray soft state have so far been seen (Safi-Harb & Kotani 2003; Band et al. 1989). Because the ejection of a massive jet blob is a rare (on average two times per year) and short (approximately 10 days) event, we only have observations for part of this jet ejection.

SS 433 shows many kinds of variability related to regular (orbital and precessional) and irregular (flaring) activities. Although precession, binary orbital, and nutation periods

(162 days, 13.08 days, and 6.28 days, respectively) are well known, a noticeable variability associated with shorter scales is poorly investigated. It is worth noting that the fast variability on a timescale of a few minutes was investigated by Zwitter et al. (1991) and Goranskij et al. (1987) in the optical *V* band. More recently, X-ray fast variability of a 50 s timescale during the flaring stage was found using *Rossi X-ray Timing Explorer* (*RXTE*) observations by Kotani et al. (2002). The power spectrum of SS 433 is well represented and approximated by power law ($P \propto \nu^{-\alpha}$) in the range of 10^{-7} to 10^{-2} Hz according to the X-ray timing data analysis performed by Revnivtsev et al. (2006). They also demonstrated that at frequencies lower than 10^{-5} Hz the same variability pattern takes place in the optical, radio, and X-ray spectral bands (see their Figure 1).

Many questions regarding the complex behavior of SS 433 during outburst states as well as the nature of this compact object and its mass are still not answered. However, there is no shortage of models which are based on radio, optical, and X-ray variations of radiation detected from SS 433 (see, e.g., Marshall et al. 2002; Fabrika 2004; Safi-Harb & Kotani 2003).

The variation in mass estimates of the compact (M_x) and optical (M_v) objects and the mass ratio ($q = M_x/M_v$) are quite broad. Kawai et al. (1989) and later Antokhina et al. (1992), using *Ginga* observations of SS 433, estimated $q \simeq 0.15$ and $q = 0.15\text{--}0.25$, respectively. On the other hand, Kotani et al. (1996) using *ASCA* observations found $q \simeq 0.06\text{--}0.31$ in the frame of the precessing jet model by taking into account thermal adiabatic cooling of the jets (Brinkmann et al. 1991). Later high-resolution observations by Gies et al. (2002) found the presence

Table 1
List of Sets (Groups) of *RXTE* Observation of SS 433

Number of Set	Dates, MJD	<i>RXTE</i> Proposal ID	UT Dates	Type of Light Curve	Ref.
R1	50191–50194	10127	1996 Apr 18–21		1
R2	50868–50907	20102, 30273	1998 Feb 24–Apr 4	Outburst	1,2
R3	52222–52238	60058	2001 Nov 9–11	Outburst	1
R4	52544.46–52544.74, 52913–52914	70416, 80429	2002 Apr 18–21		1
R5	53076–53092	90401	2004 Mar 12–28	Outburst	1, 2
R6	53239–53610	90401, 91103, 91092	2005 Jul 28–Aug 28	Outburst decay	This work
R7	54085–54096	92424	2006 Dec 17–27	Outburst decay	This work

References. (1) Filippova et al. 2006; (2) Nandi et al. 2005.

of absorption lines in the spectrum of the optical A ($\sim A7$ Ib) supergiant companion. These orbital Doppler-shifted absorption lines and stationary He II emission from the companion allowed an estimate of the mass ratio of $q = 0.35$, implying the binary masses $M_x = 4.3 \pm 0.8 M_\odot$ and $M_v = 12.3 \pm 3.3 M_\odot$ in SS 433 (see Hillwig & Gies 2008 for details). Thus, the average mass ratio inferred from this X-ray data analysis $q \leq 0.25$ is smaller than that inferred from optical observations $q \sim 0.35$.

One comes to the conclusion that in the literature there is a large variation in the mass estimates of the compact object (M_x), secondary star (M_v), and their mass ratio ($q = M_x/M_v$) in SS 433. The nature of the compact object was inferred using the mass estimate or its upper limit. No other strong arguments were used to determine the nature of the compact object in SS 433 which is an eclipsing X-ray binary system, with the primary most likely a black hole (BH), or possibly a neutron star (see, e.g., Cherepashchuk 2002).

In this work, we apply a substantially new approach for diagnosing the nature of the compact object in SS 433. In Section 2.1, we present details of radio and X-ray observations of SS 433. The analysis of X-ray spectra is shown in Section 2.2. We discuss the X-ray spectral evolution of SS 433 in Section 3. X-ray spectral properties as a function of orbital phase are investigated in Section 4. The results of timing and power spectrum analysis are presented in Section 5. We consider an interpretation of observational results and show our arguments for BH presence in SS 433 in Section 6. We present a discussion and concluding remarks in Section 7.

2. OBSERVATIONS AND DATA REDUCTION

2.1. Listing of X-ray Observations Used for Data Analysis

We analyzed the archival data collected by PCA/*RXTE* (Bradt et al. 1993) which were obtained in the time period from 1996 April to 2006 December. These data allow us to investigate SS 433 in the broad X-ray energy band (3–150 keV) during the quiescent and outburst states. The *RXTE* data for SS 433 are available through the HEASARC public archive (<http://heasarc.gsfc.nasa.gov>) at the NASA Goddard Space Flight Center (GSFC). As we have already mentioned, SS 433 shows continuous (associated with a quiet state) and sporadic (associated with an active state) variability. For investigation of the outburst state and to compare it with the quiescent state, we only selected observations during uneclipsed intervals of the binary orbital period. In fact, X-ray eclipse occurs around optical primary minima at phases $|\phi| \leq 0.1$. As a result, we only used observations taken at interval $|\phi| > 0.1$ to exclude the eclipse orbital modulation. In total, these type of observations include 90 episodes of phases that are outside of eclipses. Moreover, 27 observations during eclipses taken at different precessional and

orbital phases were used for the spectral and timing analysis of orbital modulation effects.

Precessional ephemerids were taken from Fabrika (2004). The moment of maximal separation between emission lines (T_3) was taken to be $T_3 = 2443507.47$ JD, the precessional period $P_{\text{prec}} = 162.375$ days, the orbital period $P_{\text{orb}} = 13.08211$ days, and the moment of primary optical eclipse $T_0 = 2450023.62$ JD (Goranskij et al. 1998).

Standard tasks of the HEASOFT/FTOOLS 5.3 software package were utilized for data processing. We used methods recommended by the *RXTE* Guest Observer Facility according to the *RXTE* Cookbook (see http://heasarc.gsfc.nasa.gov/docs/xte/recipes/cook_book.html). For spectral analysis, we used PCA *Standard 2* mode data collected in the 3–20 keV energy range. The standard dead time correction procedure has been applied to the data. To construct broadband spectra, HEXTE data have also been used. We subtracted background corrected in off-source observations. To exclude the channels with the largest uncertainties, only data in the 20–150 keV energy range were used for the spectral analysis. In Table 1, we list the groups of *RXTE* observations covering the source evolution from quiescent to outburst states. We also used public data from the All-Sky Monitor (ASM) on board *RXTE*. The ASM light curves (2–12 keV energy range) were retrieved from the public *RXTE*/ASM archive at HEASARC.⁵

In this paper, we have analyzed X-ray spectra during the quiescent and outburst states with reference to simultaneous radio and optical observations. The monitoring RATAN-600 Radio Telescope (2–8 GHz) data in the 1996–2006 period were provided by S. Trushkin (<http://www.sao.ru/cats/~sotr/XB/>). We also used radio observations by the Green Bank Interferometer, NRAO⁶ obtained from 1996 to 1998 at 2.25 and 8.3 GHz and simultaneous V-band photoelectric photometric observations. Details of optical telescopes, reduction techniques, and compilation methods are given by Goranskij et al. (1998).

Additionally, we analyzed the *INTEGRAL*/IBIS/ISGRI spectra in the flaring state (2004) of SS 433 that were coordinated with the *RXTE* observations. We have used version 8.0 of the Offline Science Analysis (OSA) software distributed by the *INTEGRAL* Science Data Center (ISDC, <http://isdc.unige.ch>; Corvoisier et al. 2003).

We also present a comparison of the SS 433 data with that for GRS 1915+105 obtained during *BeppoSAX* observations. We used two *BeppoSAX* detectors, the Medium-Energy Concentrator Spectrometer (MECS) and a Phoswich Detection System (PDS), for this analysis. The SAXDAS data package was utilized for performing data analysis. We process the spectral analysis in the good response energy range taking into account

⁵ http://xte.mit.edu/ASM_lc.html

⁶ <http://www.gb.nrao.edu/fgdocs/gbi/arcgbi>

Table 2
List of GRS 1915+105 Observations Used in Analysis

Satellite	ObsID	Start Time (UT)	End Time (UT)
<i>BeppoSAX</i>	209850011	2000 Apr 21 08:55:30	2000 Apr 21 15:16:47

satisfactory statistics of the source: 1.8–10 keV for MECS and 15–150 keV for PDS.

2.2. Spectral Analysis

SS 433 has long been of great interest in X-ray astrophysics, and was observed early on with many satellites such as *HEAO-1* (Marshall et al. 1979), *EXOSAT* (Watson et al. 1986), *Tenma* (Matsuoka et al. 1986), and *Ginga* (Kawai et al. 1989). Using *HEAO-1*, Marshall et al. were the first to demonstrate that SS 433 is an X-ray source. The *HEAO-1* continuum was sufficiently modeled as a thermal bremsstrahlung with $kT = 14.3$ keV, and emission due to Fe–K was detected near 7 keV. The *ASCA* satellite, which carried X-ray CCD cameras for the first time, detected many pairs of Doppler-shifted emission lines from ionized metals, such as Si, S, Ar, Ca, Fe, and Ni, originating from the twin jets (Kotani et al. 1994). The emission lines were also resolved with the *Chandra* HETGS, which were found to have Doppler widths of 1000–5000 km s⁻¹ (Marshall et al. 2002; Namiki et al. 2003; Lopez et al. 2006). The broadband continuum (up to 100 keV) is approximated by a thermal bremsstrahlung spectrum with a temperature of 10–30 keV, depending on whether SS 433 is in or out of eclipse (Kawai et al. 1989; Cherepashchuk et al. 2005). Additional complex features were detected from the *XMM* spectra, however, which could be Compton-scattered emission from the jet base (Brinkmann et al. 2005) or an iron–K absorption edge due to partial covering (Kubota et al. 2007). From the width of an eclipse in the 25–50 keV band with *INTEGRAL*, Cherepashchuk et al. (2007) and Krivosheyev et al. (2009) propose that a hot extended corona around the accretion disk is responsible for the hard X-ray emission via thermal Comptonization with a temperature of 20 keV. High-quality X-ray spectra covering the broadband are critical in establishing an interpretation of the high-energy spectra of SS 433.

In our study, we model the broadband source spectra in XSPEC using an additive model consisting of the sum of the so-called bulk motion Comptonization (BMC) model and two Gaussian line components. The BMC model is a generic Comptonization model which can be applied to upscattering of soft photons injected in a hot cloud. This model consists of two parts: the first part is a direct blackbody (BB) component and the second one is a convolution of the fraction of the BB component with a broken power law, the upscattering Green function. The spectral index of the blue wing α is much smaller than that of the red wing $\alpha + 3$. The shape of the Green function (broken power law) is generic and independent of the type of Comptonization, thermal or nonthermal. The name of the model (BMC) has only been used since 1997 (see Titarchuk et al. 1997) when the model was first applied to the case of bulk motion Comptonization. However, this model can be applied to any type of Comptonization, thermal or nonthermal, but it should be, in principle, combined with an exponential cutoff which is related to average plasma energy, for example, plasma temperature for the thermal Comptonization kT_e or kinetic energy of the matter in the case of the converging (bulk inflow) Comptonization. In this paper, we consider a scenario related to our model (see Figure 1) where the Compton cloud (CC) along with converging

flow are located in the innermost part of the source and a Keplerian disk extends from the CC to the optical companion.

As we point out, *ASCA* and *Chandra* detected many lines of various elements in the soft X-ray band of the spectrum of SS 433. Particularly, iron lines Fe xxv–Fe xxvi dominate at energies $6.5 \text{ keV} < E < 7 \text{ keV}$ and show a double structure due to jet Doppler shifts. In addition to iron line emission, one can see the line emission related to hydrogen—and helium-like ions of Mg, Si, S, Ar, Ca, and Ni which display a double structure also. These line signatures indicate that the lines are formed in the relativistic jet configuration. Along with these lines, there is an appreciable emission feature at 6.4 keV which is visible in the X-ray spectrum of SS 433 (Kotani et al. 1996; Seifina 2000). This line is not subjected to Doppler shifting. Thus, we want to emphasize that by using the forms of these lines we can see features of “moving” and “stationary” structures of material surrounding SS 433.

However, the identification and precise theoretical reproduction of the line composition with *RXTE* is problematic because of its low-energy resolution. As a test trial, we added one Gaussian component to fit the spectrum varying the width and normalization of the line and found that the width σ of this Gaussian feature ranges roughly from 0.3 to 1 keV. In quite a few cases, the spectral fits using one Gaussian component provide very wide residuals extended from 6 to 9 keV. However, after adding a second narrow Gaussian component (in the 6–9 keV range), the fit quality has been significantly improved. The energies of the first and second Gaussian components, E_{line1} and E_{line2} , are presented in Table 3. For the first Gaussian E_{line1} changes from 6.5 to 6.9 keV, while the range of the second Gaussian varies from 7.1 to 9 keV. In some cases, we see a wide residual taking place around 20 keV which can be a signature of a “high-temperature bbody-like” spectral component of temperature in the range of 4–5 keV. Thus, we use our XSPEC model as $wabs*(bmc+Gaussian+Gaussian+bbbody)$ for fitting of SS 433 spectra. In particular, we use a value of hydrogen column $N_H = 1.2 \times 10^{23} \text{ cm}^2$ which was found by Filippova et al. (2006) in calculations of the XSPEC model *wabs*.

The best-fit parameters of the source spectrum are presented in Tables 3–6. For the BMC model, the parameters are the spectral index α (photon index $\Gamma = \alpha + 1$), color temperature of the BB-like injected photons kT , $\log(A)$ related to the Comptonized fraction f ($f = A/(1+A)$), and normalization of the BB-like component N_{bmc} . We find that the color temperature kT is about 1 keV for all available *RXTE* data and thus we fix a value of kT at 1 keV. When the parameter $\log(A) \gg 1$ we fix $\log(A) = 2$ (see Tables 3 and 5), because the Comptonized fraction $f = A/(1+A) \rightarrow 1$. The variations of A do not improve fit quality any more. A systematic error of 1% has been applied to the analyzed X-ray spectra. We applied this systematic error to the analyzed *RXTE* spectra in accordance to the current version of *RXTE* Cookbook (see http://heasarc.gsfc.nasa.gov/docs/xte/recipes/cook_book.html) following recommended methods by *RXTE* Guest Observer Facility.

In Figure 1, we present a suggested geometry of the X-ray source in SS 433 (see further explanation of the geometry below).

Similar to the ordinary *bbbody* XSPEC model, the normalization N_{bmc} is a ratio of the source (disk) luminosity to the square of the distance D :

$$N_{\text{bmc}} = \left(\frac{L}{10^{39} \text{ erg s}^{-1}} \right) \left(\frac{10 \text{ kpc}}{D} \right)^2. \quad (1)$$

Table 3
Best-fit Parameters of the Spectral Analysis of PCA and HEXTE Observation of SS 433 in 3–150 keV Energy Range^a

Observational ID	MJD (day)	ϕ	ψ	$\alpha = \Gamma - 1$	$\log(A)^b$	N_{bmc}^c (L_{39}/d_{10}^2)	E_{line1} , (keV)	σ_{line1} (keV)	N_{line1}	E_{line2} , (keV)	N_{line2}^c	χ_{red}^2 (dof)	F_1/F_2^d	Rem (a)
10127-01-01-00	50191.10	0.852	0.1820	1.03(2)	2.00	3.20(3)	6.90(9)	0.66(1)	3.74(6)	8.70(4)	0.28(4)	1.17(78)	6.06/4.61	
10127-01-02-00	50192.10	0.931	0.1882	1.11(1)	2.00	2.23(3)	6.87(1)	0.73(2)	3.1(1)	8.83(5)	0.21(3)	1.27(78)	4.40/3.13	ecl
10127-01-03-00	50192.71	0.973	0.1911	1.43(3)	2.00	2.01(9)	6.89(1)	0.64(2)	2.2(1)	8.64(7)	0.19(4)	0.77(78)	3.07/1.46	ecl
10127-01-04-00	50193.06	0.005	0.1941	1.36(2)	2.00	1.87(2)	6.88(1)	0.69(2)	2.3(1)	8.75(6)	0.19(4)	1.14(78)	2.99/1.51	ecl
10127-01-05-00	50193.27	0.020	0.1950	1.38(3)	2.00	1.95(5)	6.86(2)	0.67(5)	2.2(2)	8.6(1)	0.22(9)	0.99(78)	3.25/1.87	ecl
10127-01-06-00	50193.77	0.087	0.1980	1.40(2)	2.00	2.03(2)	6.89(1)	0.63(2)	2.3(1)	8.65(6)	0.21(4)	1.21(78)	3.18/1.58	ecl
10127-01-07-00	50194.91	0.149	0.2051	1.13(1)	2.00	2.83(9)	6.88(7)	0.61(1)	3.06(8)	8.63(4)	0.2(2)	1.16(78)	5.15/3.64	
20102-01-01-00	50868.77	0.642	0.3609	0.97(2)	2.00	1.64(2)	6.59(1)	0.34(2)	1.68(7)	7.95(6)	0.23(4)	1.01(77)	3.30/2.73	
20102-01-02-00	50870.24	0.754	0.3700	1.00(1)	2.00	1.84(2)	6.54(1)	0.29(2)	1.80(8)	7.71(3)	0.39(5)	1.57(77)	3.42/2.97	
20102-01-03-00	50871.91	0.895	0.3810	1.15(2)	2.00	2.14(5)	6.56(1)	0.26(3)	1.9(1)	7.70(4)	0.47(7)	1.28(78)	3.79/2.64	ecl
20102-01-04-00	50873.18	0.991	0.3850	1.36(3)	2.00	1.67(7)	6.58(1)	0.36(2)	1.82(8)	7.95(3)	0.36(4)	1.02(78)	3.79/2.64	ecl
20102-01-05-00	50874.92	0.111	0.3988	1.19(4)	2.00	1.68(6)	6.57(2)	0.33(5)	2.1(2)	7.9(1)	0.3(1)	0.85(77)	2.74/1.84	
20102-01-06-00	50876.72	0.250	0.4099	1.19(4)	2.00	1.67(6)	6.57(2)	0.33(5)	2.1(2)	7.9(1)	0.3(1)	0.85(77)	2.73/1.80	
20102-01-01-02	50876.79	0.255	0.4104	1.20(5)	2.00	1.81(6)	6.58(3)	0.36(6)	2.2(2)	7.8(3)	0.03(1)	0.93(77)	2.90/1.94	
20102-02-01-03	50877.58	0.315	0.4152	1.11(4)	2.00	1.74(6)	6.59(2)	0.43(4)	2.4(2)	8.01(9)	0.4(1)	0.98(77)	3.01/2.21	
20102-02-01-04	50877.64	0.320	0.4156	1.36(2)	2.00	1.67(2)	6.58(1)	0.36(2)	1.82(8)	7.95(3)	0.36(4)	1.01(77)	2.60/1.32	
20102-02-01-05	50877.71	0.325	0.4160	1.18(3)	2.00	1.84(4)	6.61(2)	0.39(4)	2.23(7)	7.96(8)	0.4(1)	0.70(77)	3.01/2.10	
20102-02-01-01	50877.79	0.331	0.4165	1.14(1)	2.00	1.96(2)	6.63(1)	0.42(1)	2.37(8)	8.01(4)	0.30(5)	0.94(77)	3.34/2.45	
20102-02-01-06	50878.00	0.347	0.4178	1.09(1)	2.00	2.03(1)	6.637(6)	0.42(1)	2.53(6)	8.06(3)	0.34(3)	1.42(77)	3.51/2.75	
20102-02-01-07	50878.58	0.391	0.4214	1.18(4)	2.00	2.09(6)	6.68(2)	0.46(4)	2.5(2)	8.1(3)	0.2(1)	0.84(77)	3.41/2.42	
20102-02-01-000	50878.64	0.396	0.4218	1.14(2)	2.00	2.0(1)	6.64(8)	0.44(1)	2.41(7)	8.6(1)	0.04(2)	0.63(77)	2.84/1.89	
20102-02-01-00	50878.97	0.421	0.4238	1.12(1)	2.00	1.9(1)	6.67(8)	0.46(1)	2.44(7)	8.20(4)	0.2(3)	0.84(77)	3.52/2.42	
20102-02-01-11	50879.16	0.436	0.4249	1.09(3)	2.00	1.73(5)	6.62(1)	0.45(3)	2.24(4)	8.02(6)	0.30(7)	1.34(77)	3.02/2.32	
20102-02-01-08	50879.37	0.452	0.4263	0.99(4)	2.00	1.71(9)	6.60(2)	0.50(5)	2.6(2)	8.1(1)	0.3(1)	0.68(77)	3.33/2.81	
20102-02-01-09	50879.51	0.463	0.4271	1.13(4)	2.00	1.60(6)	6.66(1)	0.60(3)	2.8(2)	8.9(1)	0.19(6)	0.89(77)	3.04/1.92	
20102-02-01-10	50879.57	0.467	0.4275	1.22(2)	2.00	1.72(3)	6.66(1)	0.46(2)	2.4(1)	8.22(7)	0.26(5)	0.79(77)	2.85/1.82	
20102-01-07-00	50889.73	0.244	0.4902	0.86(7)	0.36(9)	0.72(3)	6.70(3)	0.59(6)	0.44(7)	8.6(1)	0.04(2)	1.03(76)	1.22/1.25	
20102-02-02-01	50897.85	0.865	0.5402	1.10(2)	2.00	1.72(3)	6.16(1)	0.45(3)	1.9(1)	8.05(5)	0.32(5)	0.79(77)	3.04/2.24	
20102-02-02-00	50898.78	0.953	0.546	1.33(1)	2.00	1.85(2)	6.60(1)	0.35(2)	1.90(8)	7.92(3)	0.38(4)	1.44(77)	3.00/1.40	ecl
30273-01-01-00	50899.72	0.007	0.551	1.39(1)	2.00	1.58(1)	6.58(1)	0.35(1)	1.81(4)	7.92(3)	0.39(4)	1.38(77)	2.49/1.21	ecl
30273-01-01-01	50900.73	0.083	0.558	1.13(1)	2.00	1.72(3)	6.56(1)	0.34(2)	1.82(8)	7.83(3)	0.29(4)	1.40(77)	3.16/2.17	ecl
30273-01-02-00	50901.74	0.162	0.5642	0.99(1)	2.00	1.74(3)	6.60(1)	0.41(2)	2.02(8)	7.92(3)	0.29(4)	1.32(77)	3.32/2.85	
30273-01-02-010	50902.74	0.239	0.5704	1.07(1)	2.00	1.93(2)	6.643(8)	0.47(1)	2.32(7)	8.12(3)	0.31(4)	1.20(77)	3.52/2.73	
30273-01-02-01	50903.06	0.263	0.5724	0.98(4)	2.00	1.98(9)	6.67(2)	0.55(5)	2.6(2)	8.3(1)	0.3(1)	0.80(77)	3.81/3.21	
30273-01-03-000	50903.73	0.314	0.5765	1.17(1)	2.00	2.01(2)	6.616(8)	0.40(1)	2.32(7)	7.98(3)	0.36(4)	1.02(77)	3.35/2.34	
30273-01-03-00	50903.99	0.334	0.5781	1.15(3)	2.00	1.98(5)	6.63(1)	0.42(3)	2.4(1)	8.13(8)	0.33(8)	0.98(77)	3.32/2.31	
30273-01-03-010	50904.72	0.390	0.5826	1.17(1)	2.00	1.90(2)	6.565(8)	0.33(7)	2.09(7)	7.80(2)	0.47(4)	0.98(77)	3.31/2.30	
30273-01-03-01	50904.99	0.410	0.5843	1.21(3)	2.00	1.90(4)	6.59(2)	0.34(4)	2.1(1)	7.88(7)	0.45(1)	0.76(77)	3.12/2.04	
30273-01-03-02	50905.20	0.427	0.5856	1.25(6)	2.00	2.01(6)	6.58(3)	0.35(7)	2.01(6)	7.8(1)	0.4(1)	1.29(77)	3.21/2.01	
30273-01-05-01	50906.00	0.487	0.5905	1.06(2)	2.00	1.86(4)	6.55(1)	0.35(3)	2.2(1)	7.94(6)	0.36(7)	1.01(77)	3.32/2.61	
30273-01-05-03	50906.13	0.498	0.5913	1.09(4)	2.00	1.93(6)	6.54(2)	0.38(5)	2.2(2)	7.8(1)	0.38(5)	1.09(77)	3.42/2.64	
30273-01-05-00	50906.79	0.548	0.5953	1.23(1)	2.00	2.00(2)	6.533(8)	0.28(1)	2.04(7)	7.7(2)	0.47(4)	0.95(77)	3.24/2.12	
30273-01-05-02	50907.13	0.574	0.5975	1.20(5)	2.00	1.98(6)	6.54(2)	0.34(5)	2.2(2)	7.9(1)	0.4(1)	0.81(77)	3.21/2.21	
60058-01-01-00	52222.29	0.105	0.7082	1.07(7)	2.00	1.97(7)	6.67(4)	0.42(7)	1.8(2)	7.9(1)	0.27(7)	0.79(77)	3.47/2.84	

Table 3
(Continued)

Observational ID	MJD (day)	ϕ	ψ	$\alpha = \Gamma - 1$	$\log(A)^b$	N_{bmc}^c (L_{39}/d_{10}^2)	E_{line1} , (keV)	σ_{line1} (keV)	N_{line1}	E_{line2} , (keV)	N_{line2}^c	χ_{red}^2 (dof)	F_1/F_2^d	Rem (a)
60058-01-02-00	52223.22	0.176	0.7139	1.19(8)	2.00	2.04(6)	6.95(4)	0.43(7)	1.3(2)	7.9(1)	0.3(1)	1.15(77)	3.22/2.53	
60058-01-03-00	52224.28	0.257	0.7205	1.22(8)	2.00	2.21(7)	6.94(1)	0.6(1)	1.3(3)	6.6(1)	0.5(3)	1.37(77)	3.42/2.61	
60058-01-04-00 ^e	52225.27	0.333	0.7266	1.07(8)	-0.5(4)	1.5(3)	7.01(1)	0.72(4)	2.7(3)	9.4(1)	0.17(9)	1.09(69)	3.33/1.73	
60058-01-05-00 ^e	52226.19	0.403	0.7323	1.06(8)	-0.5(4)	1.9(3)	7.03(2)	0.63(3)	2.5(1)	9.4(1)	0.02(9)	1.30(69)	3.91/1.95	
60058-01-06-00 ^e	52227.25	0.484	0.7388	1.07(5)	-0.1(1)	1.8(3)	7.05(1)	0.74(5)	2.6(3)	9.4(1)	0.10(9)	1.01(69)	3.74/2.13	
60058-01-07-00 ^e	52228.24	0.560	0.7449	1.30(6)	2.00	2.46(4)	6.90(1)	0.52(3)	2.1(1)	8.9(1)	0.15(8)	1.08(69)	4.15/2.69	
60058-01-08-00 ^e	52229.30	0.641	0.7515	1.31(8)	0.7(3)	2.5(1)	6.95(3)	0.55(5)	2.2(2)	8.80(4)	0.25(8)	1.20(69)	4.12/2.78	
60058-01-09-00 ^e	52230.30	0.717	0.7576	1.30(5)	0.5(2)	2.1(1)	6.92(4)	0.73(6)	2.18(3)	8.69(4)	0.25(8)	0.79(69)	3.46/2.17	
60058-01-10-00 ^e	52232.15	0.859	0.7690	1.2(1)	2.00	2.27(3)	6.96(3)	0.86(4)	3.2(3)	1.2(69)	4.15/2.74	
60058-01-11-00 ^e	52233.27	0.952	0.7758	1.20(8)	2.00	2.06(1)	6.97(4)	0.63(7)	1.9(2)	8.7(2)	0.2(1)	1.2(69)	3.57/2.37	ecl
60058-01-12-00	52234.33	0.028	0.7819	1.20(9)	2.00	1.8(1)	7.03(5)	0.68(9)	1.7(3)	8.7(2)	0.1(1)	1.04(77)	3.16/2.07	ecl
60058-01-13-00	52235.33	0.105	0.7881	1.21(8)	2.00	2.60(8)	6.95(3)	0.55(5)	2.6(8)	9.0(4)	0.2(1)	1.17(77)	4.27/3.08	ecl
60058-01-15-00 ^e	52236.18	0.167	0.7939	1.19(5)	2.00	2.58(2)	6.99(2)	0.67(4)	2.6(2)	1.09(69)	4.85/3.42	
60058-01-17-00	52238.23	0.324	0.8065	1.26(5)	2.00	3.57(7)	7.06(3)	0.69(4)	2.5(2)	1.59(71)	5.71/3.94	
70416-01-01-00	52544.46	0.732	0.6951	1.13(5)	2.00	1.60(7)	6.64(4)	0.2(1)	1.6(2)	7.9(1)	0.3(1)	0.93(72)	2.99/2.04	
70416-01-01-01	52544.66	0.747	0.6963	1.00(6)	0.4(1)	1.7(1)	6.57(6)	0.2(1)	1.2(2)	7.7(1)	0.4(1)	0.81(71)	2.76/1.98	
70416-01-01-02	52544.74	0.753	0.6968	0.97(6)	0.7(2)	1.5(1)	6.61(6)	0.3(1)	1.61(6)	7.8(1)	0.4(2)	0.87(72)	2.92/2.23	
80429-01-01-00	52913.69	0.963	0.9711	1.21(8)	2.0	1.8(1)	7.30(9)	1.2(1)	2.3(5)	1.13(72)	3.36/2.03	ecl
80429-01-01-01	52914.22	0.007	0.9761	1.22(5)	2.0	1.84(8)	7.42(5)	1.8(2)	1.06(7)	1.03(72)	3.22/1.983	ecl
90401-01-01-01 ^e	53076.78	0.423	0.9780	1.30(2)	0.4(2)	3.4(1)	7.23(3)	0.96(8)	4.7(6)	9.2(3)	0.1(1)	1.01(69)	8.59/6.54	
90401-01-01-03 ^e	53076.85	0.428	0.9784	1.30(2)	0.3(1)	3.4(1)	7.15(2)	0.80(4)	4.4(8)	9.3(2)	0.26(8)	1.03(69)	7.91/4.85	
90401-01-01-00 ^e	53077.77	0.498	0.9841	1.32(2)	0.3(1)	3.03(6)	7.06(1)	0.75(2)	4.3(2)	9.08(5)	0.30(5)	1.24(69)	7.72/4.75	
90401-01-01-02 ^e	53078.75	0.573	0.9901	1.30(1)	2.00	3.5(1)	7.02(3)	0.87(4)	4.1(4)	8.9(2)	0.1(1)	1.35(69)	7.01/4.63	
90401-01-02-01 ^e	53089.07	0.362	0.0538	1.31(2)	0.9(6)	3.4(1)	7.07(2)	0.97(4)	5.3(3)	1.17(69)	5.25/3.01	
90401-01-02-00 ^e	53089.28	0.378	0.0550	1.30(2)	1.8(1)	3.6(1)	7.12(2)	0.80(3)	4.3(1)	9.2(1)	0.80(3)	1.34(69)	8.01/5.47	
90401-01-03-01 ^e	53091.04	0.512	0.0659	1.29(2)	0.16(2)	3.2(1)	7.02(3)	0.70(7)	3.7(4)	8.8(1)	0.4(1)	1.14(69)	5.64/3.58	
90401-01-03-02 ^e	53091.82	0.572	0.0707	1.29(2)	0.4(1)	3.3(1)	7.04(2)	0.73(4)	3.8(3)	9.1(4)	0.21(9)	1.08(69)	5.95/3.51	
90401-01-03-00 ^e	53092.09	0.593	0.0724	1.31(2)	2.00	2.8(1)	7.10(2)	0.90(4)	4.2(3)	1.19(69)	5.93/3.62	
90401-01-04-01	53239.49	0.860	0.9814	1.2(1)	2.00	3.42(8)	7.33(3)	0.71(4)	2.4(1)	1.50(73)	5.62/3.98	
90401-01-05-01	53361.71	0.202	0.7352	1.00(6)	2.00	1.24(9)	6.58(2)	0.42(4)	1.8(1)	1.15(73)	2.89/2.12	
90401-01-06-00	53363.75	0.359	0.7478	1.09(2)	2.00	1.46(9)	6.60(3)	0.31(4)	1.8(1)	8.3(1)	0.27(9)	1.19(73)	2.87/1.91	
90401-01-06-01	53366.13	0.540	0.7624	0.95(7)	2.00	1.71(6)	6.62(3)	0.33(7)	2.4(2)	8.3(1)	0.4(1)	1.15(71)	3.45/2.96	
91103-01-01-00	53579.63	0.861	0.0791	1.18(3)	2.00	2.72(9)	7.09(2)	0.91(2)	3.9(3)	1.17(71)	2.78/1.63	
91103-01-09-00	53580.55	0.931	0.0848	1.19(4)	2.00	2.4(4)	7.22(4)	0.87(6)	2.1(2)	0.97(74)	4.20/2.57	ecl
91103-01-02-01	53580.83	0.952	0.0865	1.18(3)	2.00	1.88(5)	7.1(1)	0.78(2)	1.7(5)	8.7(1)	0.2(2)	1.18(73)	3.38/2.13	ecl
91103-01-02-00 ^e	53580.90	0.958	0.0870	1.18(3)	0.2(2)	2.21(2)	6.70(2)	0.27(3)	0.6(3)	8.0(2)	0.4(1)	0.97(69)	2.97/1.74	ecl
91103-01-03-00	53581.53	0.006	0.0908	0.94(6)	0.58(5)	1.6(1)	6.96(3)	0.99(3)	1.61(6)	9.3(1)	0.10(8)	1.02(73)	2.79/2.30	ecl, "A"
91103-01-04-01	53581.73	0.021	0.0920	0.92(2)	0.6(1)	1.95(1)	7.5(1)	0.9(1)	1.1(4)	6.9(1)	0.4(2)	1.04(71)	2.91/1.90	ecl
91103-01-04-00	53581.89	0.033	0.0930	0.90(6)	0.6(1)	1.5(1)	6.8(1)	1.29(1)	3.0(5)	0.85(73)	3.22/2.52	ecl
91103-01-05-00 ^e	53582.87	0.108	0.0991	1.2(1)	0.01(4)	2.5(3)	7.08(6)	0.75(8)	2.8(6)	0.97(69)	3.90/2.13	
91103-01-05-01 ^e	53582.94	0.113	0.0995	1.20(6)	0.9(1)	3.1(4)	7.02(6)	0.75(9)	3.0(6)	1.07(69)	5.41/3.34	
91103-01-07-00 ^e	53583.56	0.161	0.1034	1.2(1)	2.00	3.3(2)	7.03(3)	0.75(6)	2.8(3)	7.1(4)	0.9(2)	1.04(69)	6.30/3.88	"B"
91103-01-06-00 ^e	53583.78	0.178	0.1047	1.19(2)	2.00	3.2(3)	7.08(5)	0.90(9)	3.0(4)	7.0(1)	0.05(3)	1.25(69)	5.56/3.44	
91103-01-06-01 ^e	53584.68	0.246	0.1102	1.2(1)	2.00	3.2(3)	7.06(3)	0.75(5)	3.5(3)	7.01(8)	0.6(3)	1.03(69)	6.79/4.01	

Table 3
(Continued)

Observational ID	MJD (day)	ϕ	ψ	$\alpha = \Gamma - 1$	$\log(A)^b$	N_{bmc}^c (L_{39}/d_{10}^2)	E_{line1} (keV)	σ_{line1} (keV)	N_{line1}	E_{line2} (keV)	N_{line2}^c	χ_{red}^2 (dof)	F_1/F_2^d	Rem (a)
91103-01-08-00 ^e	53584.83	0.258	0.1112	1.2(1)	2.00	3.0(4)	7.12(9)	0.98(6)	4.1(3)	7.0(1)	0.5(3)	1.03(69)	6.56/4.29	
91103-01-09-01 ^e	53585.95	0.344	0.1181	1.2(1)	2.00	3.0(4)	6.87(6)	0.84(9)	3.9(7)	1.05(69)	6.54/4.34	
91092-01-01-00 ^e	53588.22	0.517	0.1321	1.20(3)	0.6(3)	2.71(4)	6.89(3)	0.75(6)	3.7(4)	9.1(1)	0.2(1)	0.96(69)	4.36/2.56	
91092-01-02-00 ^e	53588.35	0.527	0.1329	1.20(3)	0.14(9)	2.90(5)	6.88(1)	0.50(2)	2.8(1)	1.17(69)	5.93/3.58	
91092-02-01-02	53594.01	0.960	0.1678	1.20(3)	0.57(4)	2.11(4)	6.90(5)	0.46(7)	1.6(1)	8.3(1)	0.3(1)	1.08(73)	3.22/1.92	ecl
91092-02-01-04	53594.14	0.970	0.1686	1.12(8)	0.45(6)	2.05(4)	6.98(6)	0.52(6)	1.5(2)	8.6(1)	0.19(9)	1.08(73)	3.13/1.98	ecl
91092-02-01-00	53594.38	0.988	0.1701	1.07(3)	0.35(2)	2.0(1)	6.89(2)	0.38(2)	1.3(1)	8.37(8)	0.34(8)	1.12(73)	2.98/1.95	ecl
91092-02-01-01	53594.58	0.004	0.1713	1.10(3)	0.5(1)	1.9(1)	6.84(3)	0.36(7)	1.3(2)	7.9(7)	0.3(2)	0.70(73)	3.10/2.06	ecl
91092-02-07-01	53594.65	0.008	0.1717	1.2(1)	0.31(4)	2.0(3)	6.70(6)	0.38(8)	1.1(1)	8.3(2)	0.2(1)	1.13(71)	2.78/1.63	ecl
91092-02-01-03	53594.72	0.014	0.1722	1.05(3)	0.46(7)	1.70(9)	6.88(5)	0.60(5)	1.6(3)	8.6(1)	0.3(1)	1.04(72)	2.87/1.96	ecl
91092-02-02-00	53595.17	0.048	0.1749	1.10(3)	0.4(3)	1.7(1)	6.90(3)	0.65(6)	1.71(2)	8.72(9)	0.20(7)	1.11(72)	3.04/2.02	ecl
91092-02-03-00	53595.49	0.073	0.1769	1.16(1)	2.00(0)	1.96(5)	6.81(1)	0.57(1)	1.9(2)	8.5(1)	0.03(1)	1.28(72)	3.62/2.32	ecl
91092-02-04-00G ^e	53596.15	0.123	0.1810	1.22(3)	0.6(4)	2.7(1)	6.81(2)	0.48(5)	1.7(1)	8.37(5)	0.40(7)	1.46(69)	5.63/3.54	
91092-02-05-00 ^e	53596.34	0.138	0.1822	1.20(3)	0.5(3)	2.9(1)	6.83(1)	0.46(4)	2.6(2)	8.44(8)	1.2(4)	1.46(69)	5.29/3.57	
91092-02-06-01 ^e	53596.96	0.185	0.1860	1.22(3)	0.6(2)	2.76(9)	6.90(2)	0.53(3)	2.5(1)	8.50(8)	0.32(7)	1.04(69)	5.14/3.26	
91092-02-06-02 ^e	53597.09	0.195	0.1868	1.20(3)	2.00	3.0(2)	6.93(4)	0.54(8)	2.2(2)	8.7(3)	0.2(1)	1.02(69)	5.25/3.58	
91092-02-06-00 ^e	53597.13	0.198	0.1871	1.20(3)	1.1(4)	2.72(1)	6.80(2)	0.50(3)	2.5(1)	8.30(8)	0.43(8)	1.05(69)	5.52/3.53	
91092-02-07-00	53597.34	0.214	0.1883	1.20(3)	2.00	3.1(2)	6.88(2)	0.46(4)	2.2(2)	8.5(1)	0.17(8)	1.10(72)	5.41/3.73	
91092-02-08-00 ^e	53598.38	0.293	0.1947	1.20(1)	0.1(1)	2.64(9)	6.80(6)	0.53(2)	1.6(3)	8.3(2)	0.2(1)	1.13(71)	3.358/1.71	
91103-01-10-00	53610.77	0.241	0.2712	1.18(4)	2.00	2.59(3)	6.63(2)	0.40(4)	2.3(1)	1.08(73)	4.12/2.75	
92424-01-02-05	54085.94	0.563	0.2016	1.18(7)	2.00	2.73(5)	6.84(3)	0.59(5)	2.8(2)	1.17(73)	4.51/3.28	
92424-01-01-00	54086.99	0.643	0.2081	1.19(4)	2.00	3.11(7)	6.70(3)	0.51(8)	2.5(3)	8.2(1)	0.2(2)	1.10(71)	5.42/3.67	
92424-01-01-01	54087.97	0.718	0.2141	1.16(7)	2.00	2.95(7)	6.68(2)	0.31(3)	2.2(3)	7.9(2)	0.3(2)	1.33(71)	5.57/4.26	
92424-01-01-02	54088.95	0.793	0.2202	1.21(5)	2.00	3.13(5)	6.66(1)	0.29(7)	2.0(5)	7.8(2)	0.6(4)	1.43(71)	5.36/3.61	
92424-01-01-03	54089.92	0.867	0.2261	1.21(7)	2.00	2.64(3)	6.67(2)	0.44(4)	2.4(1)	1.43(73)	4.59/2.99	
92424-01-02-02	54093.85	0.167	0.2504	1.16(3)	2.00	2.31(4)	6.53(2)	0.16(6)	2.3(2)	7.9(1)	0.4(1)	1.22(71)	3.94/2.79	
92424-01-02-03	54094.91	0.249	0.2569	1.16(3)	2.00	2.10(4)	6.51(3)	0.32(8)	2.2(2)	7.9(1)	0.4(1)	1.30(71)	3.85/2.48	
92424-01-02-04	54095.91	0.325	0.2630	1.16(3)	2.00	2.34(6)	6.53(5)	0.23(3)	1.9(3)	7.8(3)	0.3(2)	0.93(71)	4.01/2.67	
92424-01-02-05	54096.73	0.388	0.2681	1.16(3)	2.00	2.13(5)	6.48(2)	0.05(3)	1.8(3)	7.6(1)	0.6(2)	0.86(71)	3.86/2.54	

Notes. Parameter errors correspond to 1σ confidence level. ^(a) term “ecl” marks the observations during the primary eclipse according to optical ephemerids (Goranskij et al. 1998).

^a The spectral model is $wabs * (bmc + Gaussian1 + Gaussian2)$.

^b When parameter $\log(A) > 1$, it is fixed at 2.0 (see comments in the text).

^c The normalization parameter of Gaussian1 and Gaussian2 components is in units of 10^{-3} (10^{-10} erg s $^{-1}$ cm $^{-2}$), σ_{line2} of Gaussian2 component is fixed at 0.01 keV (see comments in the text).

^d Spectral fluxes (F_1/F_2) in the 3–60/13–150 energy ranges, correspondingly, in units of 10^{-10} erg s $^{-1}$ cm $^{-2}$.

^e These observations are fitted with the $wabs * (bmc + Gaussian1 + Gaussian2 + bbody)$ model; see values of the best-fit BB color temperature and EW in Tables 4, 5, and 6.

Table 4
Best-fit Parameters of the Spectral Analysis of PCA and HEXTE Observation of SS 433 in 3–150 keV Energy Range in the Model:
 $wabs*(bmc+gaussian+gaussian+“bbody”)$ for Observations with Numbers 90401-NN-NN-NN

Model	Parameter	-01-01-00	-01-01-01	-01-01-02	-01-01-03	-01-02-00	-01-02-01	-01-03-00	-01-03-01	-01-03-02
bmc										
	Γ	2.32(2)	2.30(2)	2.30(1)	2.30(2)	2.30(2)	2.31(2)	2.31(2)	2.29(2)	2.29(2)
	kT (keV)	1.08(2)	1.15(5)	1.14(3)	1.23(5)	0.9(2)	1.18(9)	1.17(3)	1.06(4)	1.23(5)
	$\log A^a$	0.3(1)	0.4(2)	2.00	0.3(1)	1.8(1)	0.9(6)	2.00	0.16(2)	0.4(1)
	N_{bmc}^b	3.3(6)	3.4(1)	3.5(1)	3.4(1)	3.6(6)	3.4(1)	2.8(1)	3.2(1)	3.3(1)
Gaussian1										
	E_{line1} (keV)	7.06(1)	7.23(3)	7.02(3)	7.15(2)	7.12(2)	7.07(2)	7.10(2)	7.02(3)	7.04(2)
	σ_{line1} (keV)	0.75(2)	0.96(8)	0.87(4)	0.80(4)	0.80(3)	0.97(4)	0.90(4)	0.70(7)	0.73(4)
	N_{line1}^b	4.3(2)	4.7(6)	4.1(4)	4.4(8)	4.3(1)	5.3(3)	4.2(3)	3.7(4)	3.8(3)
Gaussian2										
	E_{line2} (keV)	9.08(5)	9.2(3)	8.9(2)	9.3(2)	9.2(1)	8.8(1)	...
	N_{line2}^b	0.30(5)	0.1(1)	0.1(1)	0.26(8)	0.80(3)	0.4(1)	...
“bbody”										
	$T_{“bbody”}$ (keV)	5.5(1)	5.9(2)	5.9(3)	5.3(1)	5.4(4)	5.7(4)	6.4(6)	5.4(4)	5.3(5)
	$N_{“bbody”}^b$	3.2(1)	3.6(3)	2.8(5)	4.3(4)	3.3(5)	3.3(4)	1.9(3)	1.9(3)	1.1(2)
	EW _{“bbody”}} (keV)	1.4(2)	1.4(3)	1.4(5)	1.4(5)	1.4(1)	1.4(2)	1.4(1)	1.4(2)	1.2(1)
Flux ^c										
	3–60 keV	5.18	5.48	5.01	4.76	7.79	5.51	5.26	6.79	5.56
	13–150 keV	2.84	2.99	2.69	2.30	4.65	3.02	3.03	4.02	3.38
	χ^2 (dof)	1.24(69)	0.98(69)	1.15(69)	1.03(69)	0.97(69)	1.05(69)	1.13(69)	1.14(69)	1.08(69)

Notes. Parameter errors correspond to 1σ confidence level.

^a When parameter $\log(A) > 1$, it is fixed at 2.0 (see comments in the text).

^b Normalization in units of 10^{-3} (10^{-10} erg s $^{-1}$ cm $^{-2}$).

^c Spectral flux in units of 10^{-10} erg s $^{-1}$ cm $^{-2}$ and σ_{line2} for the Gaussian2 component was fixed at 0.01 keV.

Table 5
Best-fit Parameters of the Spectral Analysis of PCA and HEXTE Observation of SS 433 in 3–150 keV Energy Range in the Model:
 $wabs*(bmc+gaussian+gaussian+“bbody”)$ for Observations with Numbers 91103-NN-NN-NN

Model	Parameter	-01-02-00	-01-05-00	-01-05-01	-01-06-00	-01-06-01	-01-07-00	-01-08-00	-01-09-01
bmc									
	Γ	2.18(3)	2.2(1)	2.20(6)	2.19(5)	2.2(1)	2.21(1)	2.2(1)	2.2(1)
	kT (keV)	1.04(1)	1.29(8)	1.25(6)	1.22(7)	1.23(6)	1.21(4)	1.18(7)	1.11(9)
	$\log A^a$	0.2(2)	0.01(4)	0.9(1)	2.0	2.0	2.0	2.0	2.0
	N_{bmc}^b	2.21(2)	2.5(3)	3.1(4)	3.2(3)	3.2(3)	3.3(2)	3.0(4)	3.0(4)
Gaussian1									
	E_{line1} (keV)	6.70(2)	7.08(6)	7.02(7)	7.08(5)	7.06(3)	7.03(3)	7.12(9)	6.87(6)
	σ_{line1} (keV)	0.27(3)	0.75(8)	0.75(9)	0.90(9)	0.75(5)	0.75(6)	0.98(6)	0.84(9)
	N_{line1}^b	0.6(3)	2.8(5)	3.0(5)	3.0(4)	3.5(3)	2.8(3)	4.1(3)	3.9(7)
Gaussian2									
	E_{line2} (keV)	8.0(2)	7.0(1)	7.01(8)	7.1(4)	7.0(1)	...
	N_{line2}^b	0.4(1)	0.05(3)	0.6(3)	0.9(2)	0.5(2)	...
“bbody”									
	$T_{“bbody”}$ (keV)	4.9(2)	4.9(2)	4.9(4)	5.1(9)	5.1(3)	5.6(5)	5.2(4)	5.5(3)
	$N_{“bbody”}^b$	1.17(7)	2.1(6)	1.2(8)	0.8(6)	2.6(5)	1.7(4)	1.9(4)	2.3(6)
	EW _{“bbody”}} (keV)	1.2(2)	1.3(3)	1.4(5)	1.4(5)	1.4(1)	1.4(2)	1.4(1)	1.4(2)
Flux ^c									
	3–60 keV	4.99	3.90	5.41	5.56	6.72	6.30	6.56	6.54
	13–150 keV	3.17	2.13	3.34	3.44	4.01	3.88	4.29	4.34
	χ^2 (dof)	1.17(69)	0.97(69)	1.05(69)	1.25(69)	1.01(69)	1.04(69)	1.03(69)	1.05(69)

Notes. Parameter errors correspond to 1σ confidence level.

^a When parameter $\log(A) > 1$, it is fixed at 2.0 (see comments in the text).

^b Normalization in units of 10^{-3} (10^{-10} erg s $^{-1}$ cm $^{-2}$).

^c Spectral flux in units of 10^{-10} erg s $^{-1}$ cm $^{-2}$ and σ_{line2} for the Gaussian2 component was fixed at 0.01 keV.

Table 6
Best-fit Parameters of the Spectral Analysis of PCA and HEXTE Observation of SS 433 in 3–150 keV Energy Range in the Model: $wabs*(bmc+gaussian+gaussian+“bbody”)$ for Observations with Numbers 91092-NN-NN-NN

Model	Parameter	-01-01-00	-01-02-00	-02-04-00G	-02-05-00	-02-06-00	-02-06-01	-02-08-00
bmc	Γ	2.20(3)	2.20(3)	2.22(3)	2.2(3)	2.22(1)	2.22(3)	2.20(1)
	kT (keV)	1.1(1)	1.22(3)	1.20(6)	1.28(6)	1.21(7)	1.3(1)	1.35(2)
	$\log A^a$	0.6(3)	0.1(1)	0.6(4)	0.5(3)	1.2(1)	0.6(2)	0.1(1)
	N_{bmc}^b	2.71(2)	2.90(5)	2.7(1)	2.9(1)	2.6(2)	2.67(9)	2.64(9)
Gaussian1	E_{line1} (keV)	6.89(3)	6.88(1)	6.81(2)	6.83(1)	6.90(2)	6.90(2)	6.80(6)
	σ_{line1} (keV)	0.75(6)	0.50(2)	0.48(5)	0.46(4)	0.51(5)	0.53(3)	0.53(2)
	N_{line1}^b	3.7(4)	2.8(1)	1.7(1)	2.6(2)	2.4(2)	2.5(1)	1.6(3)
Gaussian2	E_{line2} (keV)	9.1(1)	...	8.37(5)	8.44(1)	8.4(9)	8.50(8)	8.3(2)
	N_{line2}^b	0.2(1)	...	0.40(7)	1.2(4)	2.3(9)	0.32(7)	0.21(2)
“bbody”	$T_{“bbody”}$ (keV)	4.5(2)	4.5(2)	4.4(4)	4.9(6)	5.5(5)	5.0(4)	4.5(4)
	$N_{“bbody”}^b$	1.7(7)	2.2(4)	1.3(4)	2.8(5)	1.9(6)	1.7(1)	1.9(3)
	EW _{“bbody”}} (keV)	1.2(2)	1.3(3)	1.4(5)	1.4(5)	1.4(1)	1.4(2)	1.4(1)
Flux ^c	3–60 keV	4.36	4.07	4.42	4.43	3.61	3.98	3.35
	13–150 keV	2.56	2.44	2.80	2.90	1.46	1.81	1.71
	χ^2 (dof)	0.96(69)	1.07(69)	1.39(69)	1.06(69)	1.05(69)	0.96(69)	1.05(69)

Notes. Parameter errors correspond to 1σ confidence level.

^a When parameter $\log(A) > 1$, it is fixed at 2.0 (see comments in the text).

^b Normalization in units of $10^{-3}(10^{-10} \text{ erg s}^{-1} \text{ cm}^{-2}) \times 10^{-3}$.

^c Spectral flux in units of $10^{-10} \text{ erg s}^{-1} \text{ cm}^{-2}$ and σ_{line2} for the Gaussian2 component is fixed at 0.01 keV.

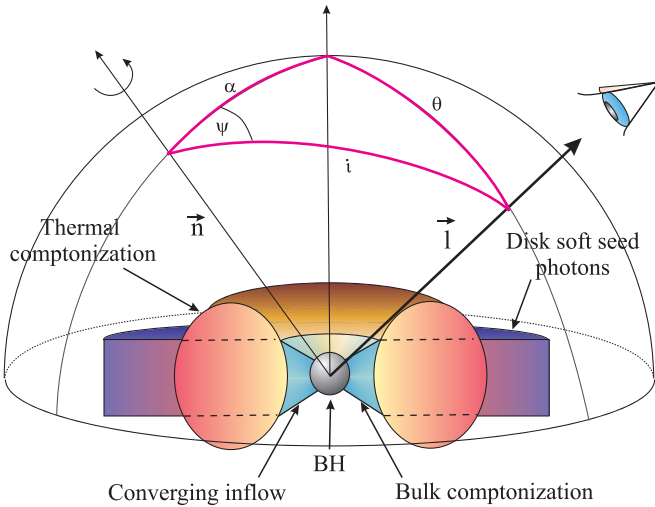


Figure 1. Schematic view of the proposed geometry for thermal and bulk Comptonization regions in the source SS 433 hosting a BH with a power-law-like emission at high energies. The terminal direction of viewing of the central disk part to the Earth observer is marked by vector \vec{l} . Here, vector \vec{n} is denoted normal to the orbital plane, i is an inclination angle, ψ is a precession phase angle, and α is the cone precession angle, and a bended arrow points the direction of the disk precession motion around normal \vec{n} to the orbital plane.

(A color version of this figure is available in the online journal.)

The adopted spectral model shows a very good performance throughout all of the data set used in our analysis, namely, the value of reduced χ^2 -statistic $\chi_{red}^2 = \chi^2/N_{dof}$, where N_{dof} is the number of degrees of freedom for a fit, is less than or around 1.0 for most observations. A small fraction (less than 2%) of the

spectra with a high counting statistic χ_{red}^2 reach 1.5. However, they never exceed a rejection limit of 2.0.

3. EVOLUTION OF SS 433 X-RAY SPECTRA DURING OUTBURSTS

We have established general tendencies of the quiescent-outburst behavior of SS 433 based on spectral parameter evolution of X-ray emission in the energy range 3–150 keV using *RXTE*/P-CA/HEXTE data. We have also found a correlation between the X-ray emission of SS 433 and radio patterns observed by RATAN-600 in the range 1–11 GHz and by the Green Bank Interferometer at 2.25 and 8.3 GHz.

We identified common features of the outburst behavior of SS 433 based on three available outbursts and on two outburst decay sets. According to general BH state classification (see, for example, Shaposhnikov & Titarchuk 2009, hereafter ST09), SS 433 is mostly seen in the intermediate state (IS). Different patterns of SS 433 X-ray spectra are listed in Table 3: (1) IS spectra with $\Gamma \sim 1.9$ –2.2 (see also the lower panel of Figure 2); and (2) the sum of the BMC spectrum with $\Gamma \sim 2.2$ –2.3 and a high-temperature “bbody” component found in the 10–50 keV energy range (see Figures 3 and 4).

Ten days before the radio outburst, SS 433 being in IS, a stable low soft (ASM) X-ray flux (see Figure 5) is followed by an X-ray flux rise, reaching its maximum just two days before the radio flare. Probably, at the moment of radio peak, MJD = 50890, the X-ray flux reaches its minimum (BMC normalization, $N_{BMC} \sim 0.7 \times 10^{-3}$) when the X-ray spectrum becomes harder (photon index $\Gamma \sim 1.9$). It is worth noting that the spectral index of radio emission α_{radio} has its maximal value at a time close to the X-ray outburst (see Figure 5 at MJD =

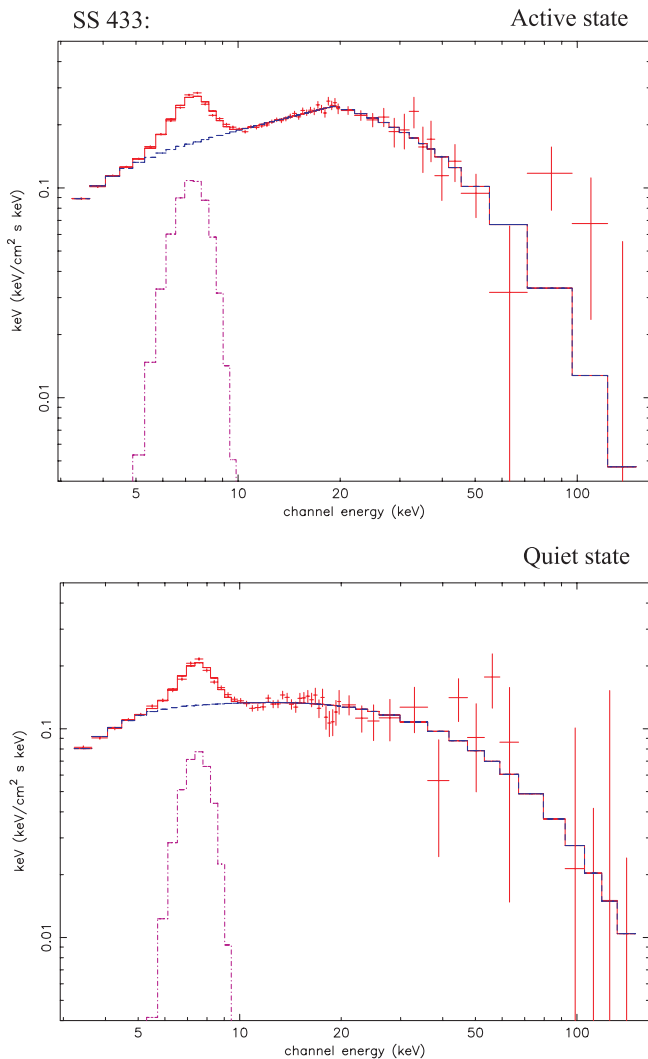


Figure 2. Two representative spectra of SS 433 in $E \times F(E)$ units for outburst IS (top) and for quiet IS (bottom). The blue line presents XSPEC continuum component of the best-fit model (see the text).

(A color version of this figure is available in the online journal.)

50886). Note that the radio spectrum is harder just a few days before the radio maximum. Then, after several days of the radio maximum, we see that the X-ray flux increases while the radio flux substantially decreases, at least by a factor of 2 (see Figure 5 and Table 3).

In Figures 6 and 7, we demonstrate an evolution of the radio, X-ray flux, and X-ray spectral parameters N_{bmc} and Γ with time for different time intervals. Notably, in Figure 6 we present the best-fit color temperature related to the “high-temperature BB” bump which is sometimes seen in IS spectra. In Figures 5–7 we also show a transition between intermediate and soft states given that the photon index varies between 1.9 and 2.4.

Thus, in Figures 5–7, we present the behavior of SS 433 during corresponding outbursts and spectral transitions using (1) the BMC normalization, (2) the photon index, (3) ASM X-ray flux, and sometimes when they are available, (4) GBI/RATAN-600 radio flux, and (5) radio spectral index (in the case of GBI observations) and the color temperature (in the case of the occurrence of a “high-temperature BB”-like feature).

The diagram of photon index Γ versus BMC-normalization forms the track shown in Figure 8 for all observations except for the ones during orbital eclipses. The rising part of the

correlation is seen in both precession periods and outburst transitions. The upper saturation part of the correlations is only seen during outburst transitions. Note that in the cases of different outbursts of SS 433 the levels of photon index saturation are also different. For example, the 2004 outburst (blue square) shows the saturation level around $\Gamma \sim 2.3$, while the 2005–2006 outbursts (crimson and red circles) saturate at a lower level of $\Gamma \sim 2.2$. Comptonization fraction f shown in the right-hand panel of Figure 8 is high in most of the cases. This means that in most cases the soft disk radiation of SS 433 is subjected to reprocessing in a CC and only a small fraction of the disk emission component ($1 - f$) is directly seen. Thus, the energy spectrum of SS 433 during all states is dominated by a Comptonized component seen as a power-law hard emission in the energy range from 3 to 70 keV, while the direct disk emission is not seen in all detected spectra.

4. SPECTRAL PROPERTIES AS A FUNCTION OF ORBITAL PHASE

4.1. Detection of “High-temperature BB-like” Bump

The “BB-like” feature has been found in 24 spectra of SS 433 among all available data (R2, R3, R5–R7). Note that during the 2004 outburst (R5 set) the “high-temperature BB-like” bump found in 10–40 keV energy range of *RXTE* has also been detected by the ISGRI/IBIS detector on board the *INTEGRAL* satellite simultaneously with the *RXTE* observation (ID 90401-01-01-01). For two time intervals (MJD = 52225–52238, 53579–53588), this feature is detected in spectra near the primary eclipse. It has been visible before and after the primary eclipse, while it is not seen during the central phases of the primary eclipse. This screening effect with respect to orbital phases is clearly seen in the two lower panels (E3 and E4) of Figure 9. The blue vertical strip marks the interval of the primary eclipse made according to optical ephemerids (Goranskij et al. 1998). Points marked with pink halos correspond to spectra fitted by the model that includes a “high-temperature BB-like” component (for details, see Figures 3 and 4 and Tables 4–7). The red points in Figure 9 (see lower two panels) correspond to observations during primary eclipse when the “BB-like” component is not seen, while it has been found before and after the eclipse. Although observations are distributed more or less uniformly with the precession phase, the “BB” bump feature is seen generally at the “disk face-on” position ($\psi = 0.75$ (E3), $\psi = 0$ (E4), Figure 9), when the precessing disk is open and the innermost part of the disk is more visible to the Earth observer.

Thus, we argue that the “BB-like” feature is better detected at the “disk face-on” position ($\psi \rightarrow 0$) than during other precession phases. Moreover, we have found the total eclipse of the “BB” bump during the primary eclipse when the compact object is obscured by the normal star. In other words, we suggest that localization of “BB” bump feature emission should be better identified during the direct observation of the innermost source region near the compact object (CC).

However, this “BB” component can be smeared out by photon scattering if the optical depth of CC is much greater than 1. That could be the case during observations for MJD = 50191–50194 (E1) and 50897–50907 (E2) (see Figure 9).

4.2. Softening of Spectra at Some Particular Orbital Phases

The relative softening of the spectrum was found in the range of $\varphi = 0.95$ –1.1 for two orbital cycles of SS 433 (see Figure 9). Softening of X-ray spectra is seen when the

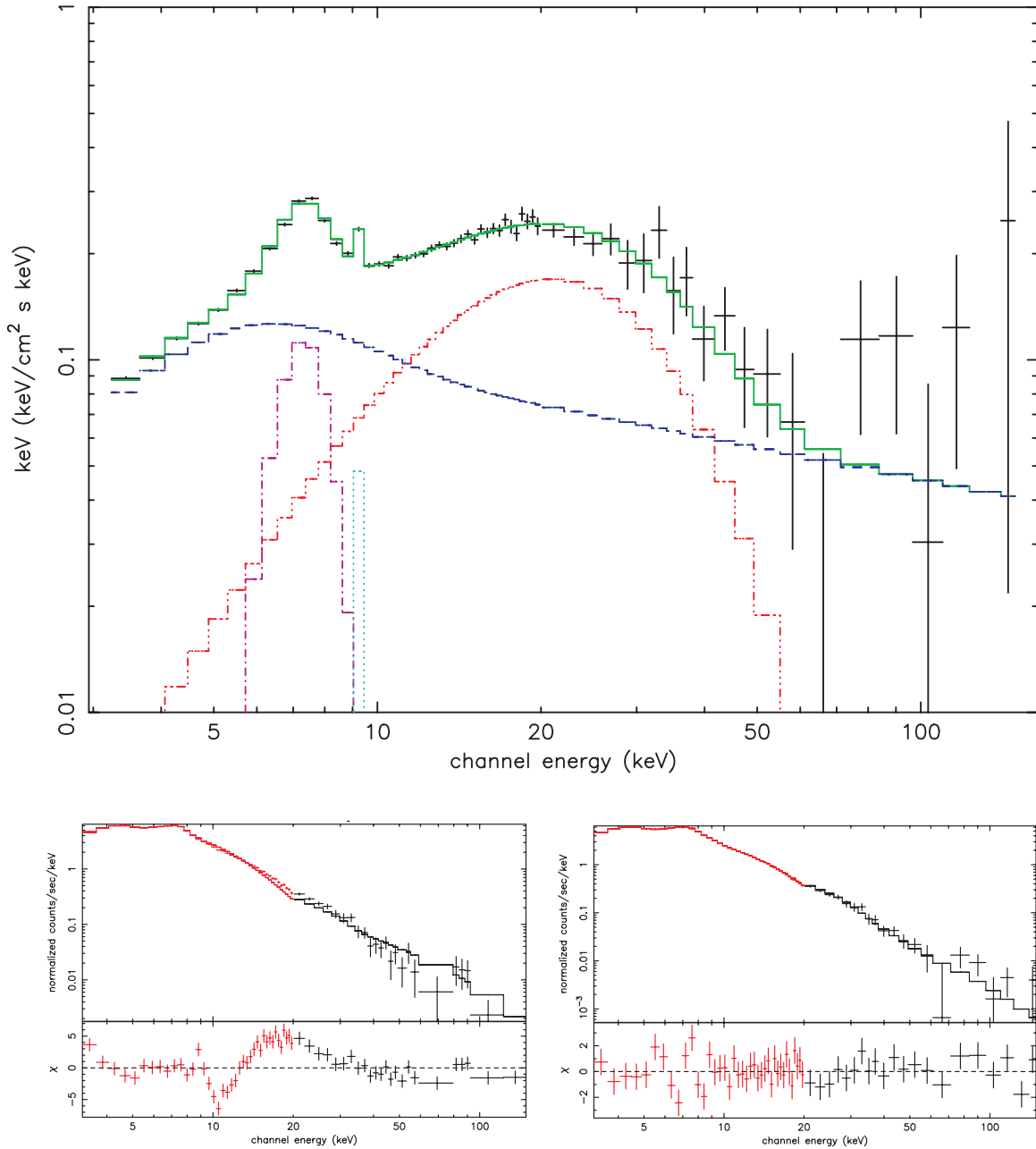


Figure 3. Best-fit spectrum during the 2004 outburst transition in $E \times F(E)$ units (top panel) and in normalized counts units (bottom panel) with χ for the 90401-01-01-01 observation (R5 set). Left: the best fit which does not include a high-temperature “bbody” component ($\chi_{\text{red}}^2 = 4.05$ for 72 dof). Right: the best-fit spectrum and $\Delta\chi^2$, when residual hump at 20 keV is modeled by a high-temperature “bbody” component with $T_{\text{BB}} = 5.9 \pm 0.2$ keV ($\chi_{\text{red}}^2 = 1.00$ for 70 dof). In the top panel, data are denoted by black points. The model consists of four components shown by blue, dashed purple, light blue, and red lines for *BMC*, *Gaussian1*, *Gaussian2*, and *bbody* components, respectively.

(A color version of this figure is available in the online journal.)

Table 7
BH Masses and Distances

Source	M_{dyn}^a (M_{\odot})	i_{orb} (deg)	i_{scal} (deg)	D^b (kpc)	M_{scal} (M_{\odot})	D_{scal} (kpc)	Refs
GX 339–4	>6	...	70	7.5 ± 1.6	12.3 ± 1.4	5 ± 0.5	1, 2
SS 433	4.3 ± 0.8	78.7	80	5.0 ± 0.5	$\gtrsim 2$...	3, 4, 5

Notes.

^a Dynamically determined BH mass.

^b Source distance found in the literature.

References. (1) Munoz-Darias et al. 2008; (2) Hynes et al. 2004; (3) Romney et al. 1987; (4) Hillwig & Gies 2008; (5) Margon 1984.

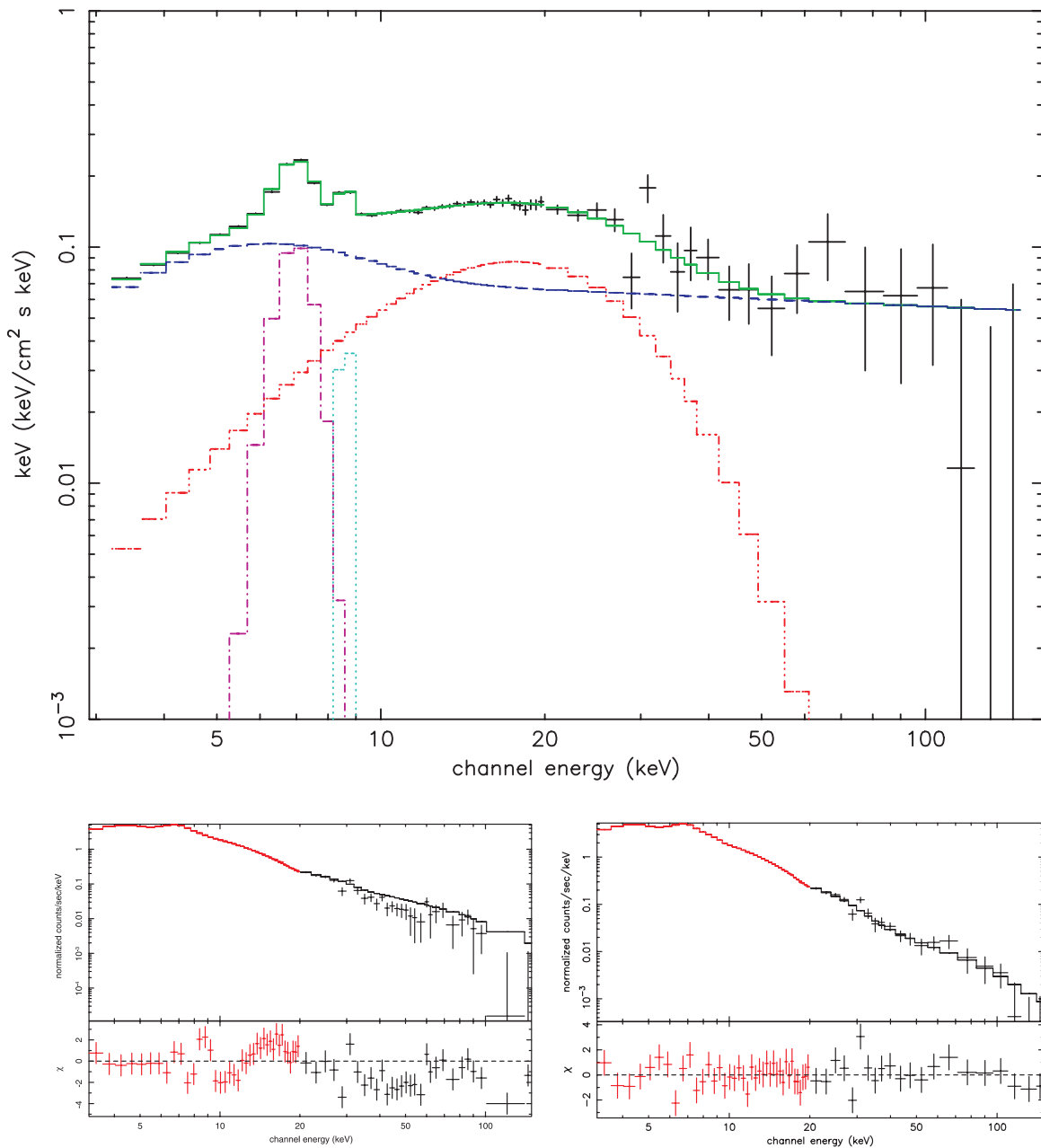


Figure 4. Best-fit spectrum during the 2005 outburst transition in $E \times F(E)$ units (top panel) and in normalized counts units (bottom panel) with χ for the 91092-01-01-00 observation (R6). Left: the best fit which does not include a high-temperature “bbody” component ($\chi_{\text{red}}^2 = 5.01$ for 72 dof). Right: the best-fit spectrum and $\Delta\chi^2$, when residual hump around 14 keV is modeled by a high-temperature “bbody” component with $T_{\text{BB}} = 4.5 \pm 0.2$ keV ($\chi_{\text{red}}^2 = 1.07$ for 70 dof). In the top panel, data are denoted by black points. The model consists of four components shown by blue, dashed purple, light blue, and red lines for *BMC*, *Gaussian1*, *Gaussian2*, and *bbody* components, respectively.

(A color version of this figure is available in the online journal.)

compact hard emitting region, presumably related to the central parts of the disk, is obscured by the donor (optical) star and thus the normalization of X-ray spectrum is suppressed due to the eclipse. This relative spectral softening is clearly seen at MJD = 50191–50194 (E1) and 50897–50907 (E2) (see the two upper panels of Figure 9) when the noticeable increase of photon index at MJD = 50192.7 ($\Gamma = 2.43 \pm 0.03$) occurs with respect to that during the rest of the eclipse interval ($\Gamma = 2.11 \pm 0.01$; see panel E1 in Figure 9). The similar behavior of the index is seen in the E2 panel where a noticeable increase of the photon index $\Gamma = 2.39 \pm 0.01$ takes place at MJD = 50899.7 compared to that when $\Gamma = 2.13 \pm 0.01$ during the rest of the eclipse interval.

5. TIMING ANALYSIS

The *RXTE* light curves were analyzed using the *powspec* task from FTOOLS 5.1. The timing analysis *RXTE*/PCA data were performed in the 2–15 keV energy range using the *binned* mode. We generated power density spectra (PDSs) with 16 s time resolution. We subtracted the contribution due to Poissonian statistics. To model PDS, we used the QPD/PLT plotting package.

We also analyzed optical and radio light curves to compare them with the X-ray curve. Timing analysis of all available data of SS 433 demonstrates power-law PDSs of index around 1.5 in three energy bands (see Figure 10): X-ray (blue), 2.25 GHz

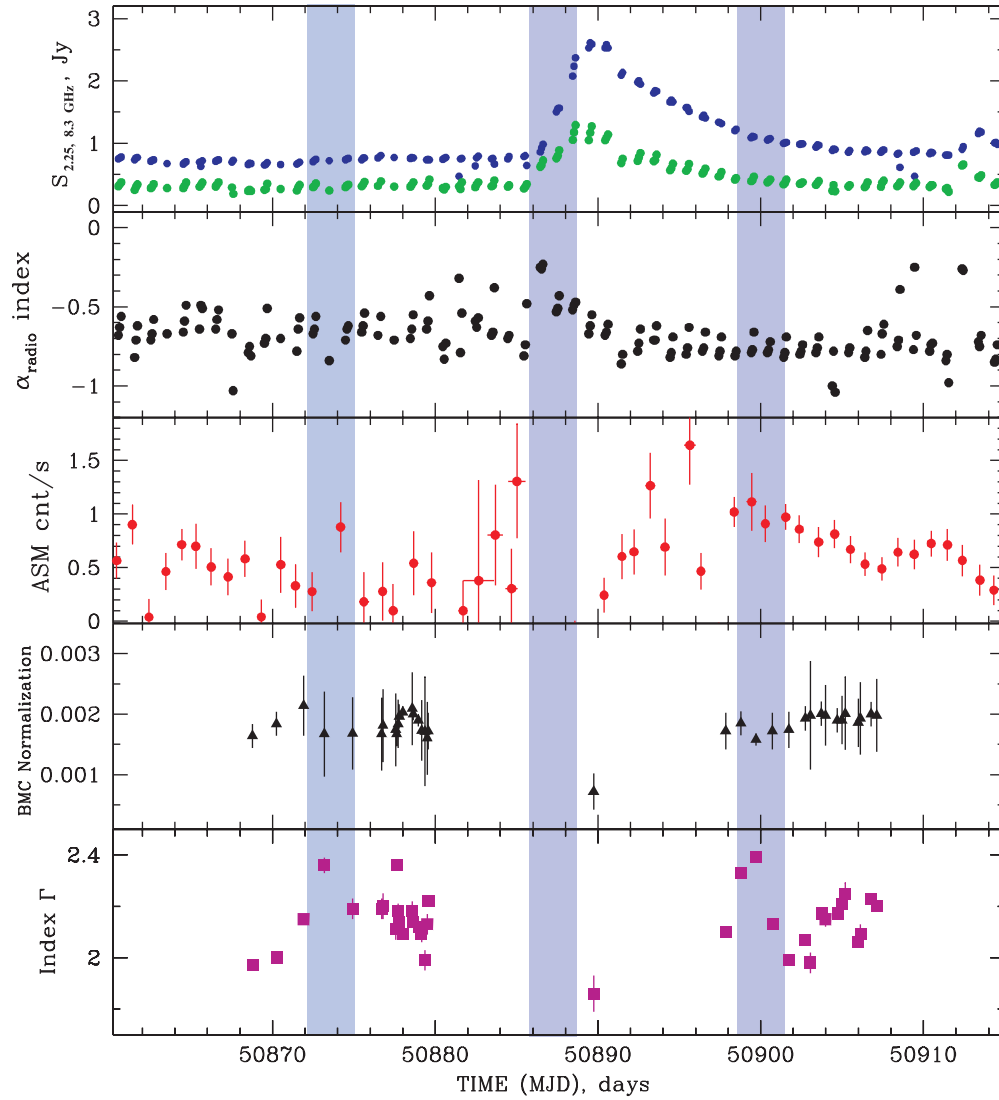


Figure 5. From top to bottom: evolution of the flux density (GBI; 2.25 GHz—blue; 8.3 GHz—green), *RXTE*/ASM count rate, spectral index α_{radio} in the corresponding radio GBI range, BMC normalization, and photon index Γ for the middle of the 2004 outburst of SS 433. Blue strips mark eclipsed intervals of light curves (around MJD 50872–50875, 50886–50889, and 50899–50902).

(A color version of this figure is available in the online journal.)

radio (black), and *V* optical (red). This result is in agreement with previous results by Revnivtsev et al. (2006), who found that the SS 433 power spectra of radio, optical, and X-ray variabilities continue with the same power law from 10^{-7} Hz up to 10^{-5} Hz.

Such an extended behavior of power spectra is well known for a number of X-ray binaries. For instance, Churazov et al. (2001) found that Cyg X-1 demonstrated a similar power-law component at 10^{-5} to 10 Hz in the X-ray energy band. An extensive study of low-mass X-ray binary (LMXB) systems showed that such a power-law behavior is common and often observed in LMXBs (see, e.g., Gilfanov & Arefiev 2005 and Titarchuk et al. 2007).

The observed variability of SS 433 in different spectral bands was interpreted in the framework of self-similar accretion disk variations suggested by Lyubarskii (1997). In particular, he proposed that when the variable mass accretion rate generates energy release in the disk far away from a compact object, the corresponding radiation should be seen in the optical and UV energy range, whereas the energy emitted in X-ray should be released near the compact object. In SS 433, presumably these mass accretion rate fluctuations are detected and observed in

the PDS. In addition, one can also see that the X-ray variability correlates with the optical and radio emissions (see Figure 10).

A study of orbital modulation allows us to detect some changes of the power spectrum of SS 433 in the energy range 3–15 keV during the primary eclipse. In the lower panel of Figure 11, we show details of the typical evolution of X-ray timing and spectral characteristics during the primary eclipse. The top panels of this figure demonstrate *V*-band optical light curve, BMC normalization, and photon index Γ for R6 set as a function of time (see Table 1 for details of these observations). In the plot of photon index Γ versus time, points A and B correspond to moments MJD = 53581 and 53585, during and after eclipse, respectively. The blue strips mark eclipsed intervals of light curve. It is worth noting that the optical and X-ray fluxes drop significantly during the primary eclipse (see the upper two panels and Table 3).

In Figure 11, PDSs (left bottom panel) are plotted along with the energy spectrum $E \times F(E)$ (right bottom panel) for two observational points A (91103-01-03-00, blue) and B (91103-01-07-00, red). The differences of the presented PDSs and energy diagrams related to events A and B are noticeable.

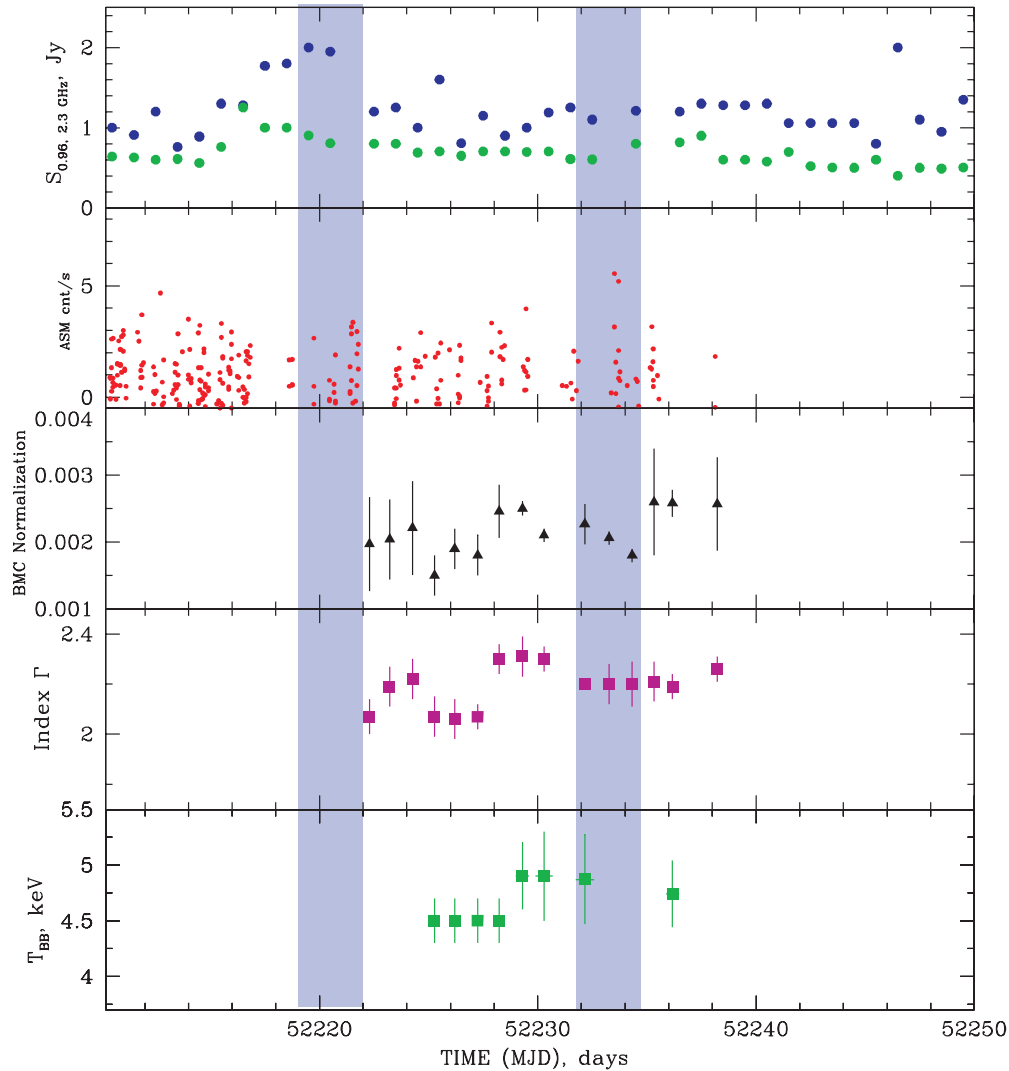


Figure 6. From top to bottom: evolution of the flux density (0.96 (green) and 2.3 (blue) GHz), RATAN-600, *RXTE*/ASM count rate, BMC normalization, photon index Γ , and the color temperature T_{BB} of high-temperature “BB” spectral component for the middle of the 2001 outburst of SS 433. Blue strips mark eclipsed intervals of light curve around MJD 52219–52221 and 52222–52234 during R3 set.

(A color version of this figure is available in the online journal.)

The PDS during the eclipse related to point A (blue histogram) indicates some weakening of power at 0.001–0.01 Hz in comparison with that for the PDS outside of the eclipse, at point B (red histogram). The corresponding spectrum during the eclipse (blue line) demonstrates a significant decrease of total flux and also of the BMC normalization, at least by a factor of 2.

6. INTERPRETATION OF OBSERVATIONAL RESULTS

Before proceeding to the interpretation of the observations, let us briefly summarize our results as follows. (1) The spectral data of SS 433 are well fitted by a BMC model plus two Gaussian and “high-temperature bbody” components (see Section 2.2). (2) The power-law spectral index of the BMC component rises and saturates with an increase of the BMC normalization (disk flux). The photon index saturation levels of the 2004 and 2005–2006 outbursts are about 2.2 and 2.3, respectively (see Figure 8). (3) There is a total eclipse of “high-temperature BB-like” feature in the photon spectrum because this spectral feature is presumably formed in the innermost part of the X-ray source and thus it should not be seen during the primary eclipse. (4) The spectral

index (hardness) clearly changes during the primary eclipse (see panels E1 and E2 in Figure 9 and one of the upper panels in Figure 11). This can be explained if there is a slight variation in spectral shape with radius through the X-ray spectral formation region.

6.1. Index Saturation as a BH Signature: BH Mass in SS 433

We have firmly established that the photon index of the resulting spectrum of SS 433 saturates with the BMC normalization $N_{\text{bmc}} \propto L_d$ or with disk mass accretion rate. ST09 presented strong arguments that this index saturation is a signature of converging flow into BH. In fact, the spectral index α is inversely proportional to the Comptonization parameter Y which is proportional to the product of the average number of photon scattering in CC, N_{sc} , and the mean efficiency of gaining energy at any scattering η . Because the index saturates, it means η is an inverse of N_{sc} . But in general, for an optically thick CC of optical depth $\tau \gg 1$ the average number of scatterings, N_{sc} , is proportional to τ^2 or τ (see, e.g., Laurent & Titarchuk 1999). In the case of thermal Comptonization, $N_{\text{sc}} \propto \tau^2$ and then η should be inversely proportional to τ^2 . But in the

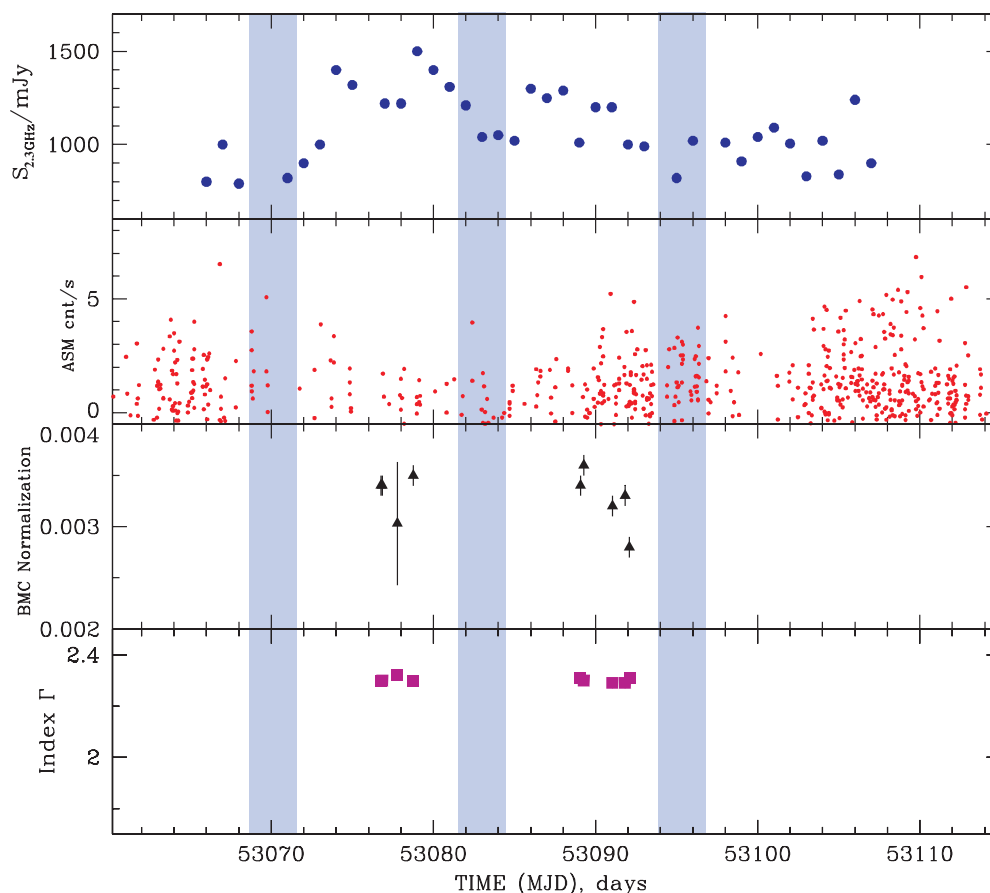


Figure 7. From top to bottom: evolution of the flux density (2.3 GHz, RATAN-600), *RXTE*/ASM count rate, BMC normalization, and photon index Γ for the middle of the 2004 outburst of SS 433. Blue strips mark eclipsed intervals of light curve around MJD 53070–53100 (R5 set). (A color version of this figure is available in the online journal.)

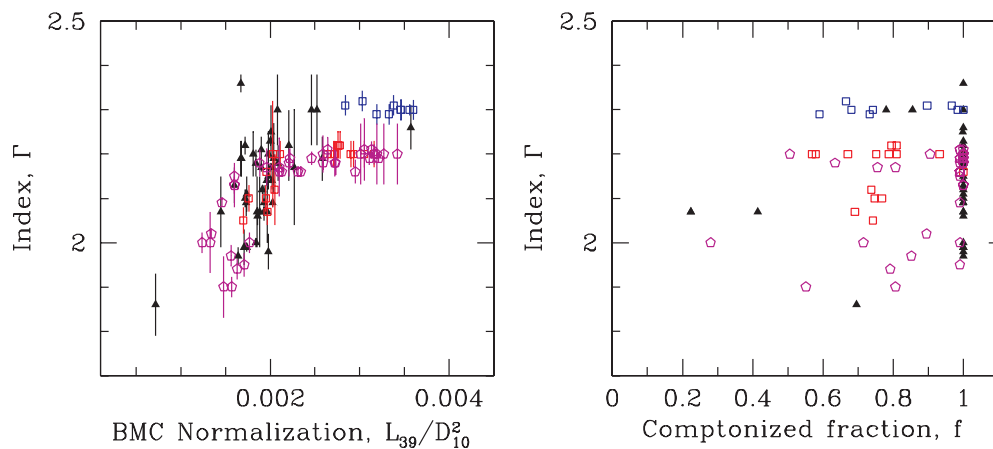


Figure 8. Photon index Γ plotted vs. BMC normalization (left) and Comptonized fraction (right) for all observations. Blue squares correspond to the 2004 outburst. Crimson circles mark 2005–2006 observations. Red squares are selected for the decay of 2005 events. Black triangles denote the rest of the observations. (A color version of this figure is available in the online journal.)

thermal Comptonization case, the efficiency η is proportional to the electron temperature kT_e only (see, e.g., Sunyaev & Titarchuk 1980) and it is not clear why there could be such a sophisticated tuning in the CC that kT_e steadily decreases with τ as τ^{-2} . On the other hand, $N_{sc} \propto \tau$ and $\eta \propto 1/\tau$ in the converging flow case (see, e.g., Titarchuk et al. 1997 and ST09) and thus the index saturation is a natural consequence of these laws for N_{sc} and η in the case of converging flow (see Titarchuk & Zannias 1998 for the solution of the full relativistic kinetic equation). Furthermore, ST09 demonstrate that for a number of black

hole candidate (BHC) sources the index saturates not only when the mass accretion rate increases but also when quasi-periodic oscillation (QPO) frequency increases. These index correlations and saturations with QPO frequency are direct evidence that the index saturation takes place when the size of CC becomes more compact (namely, the index saturates when the compactness of the emission area increases).

Titarchuk et al. (1998) demonstrated that the CC compactness increases with the mass accretion rate, \dot{M} . Moreover, in the BH case the shape of the emergent spectrum saturates, when \dot{m}

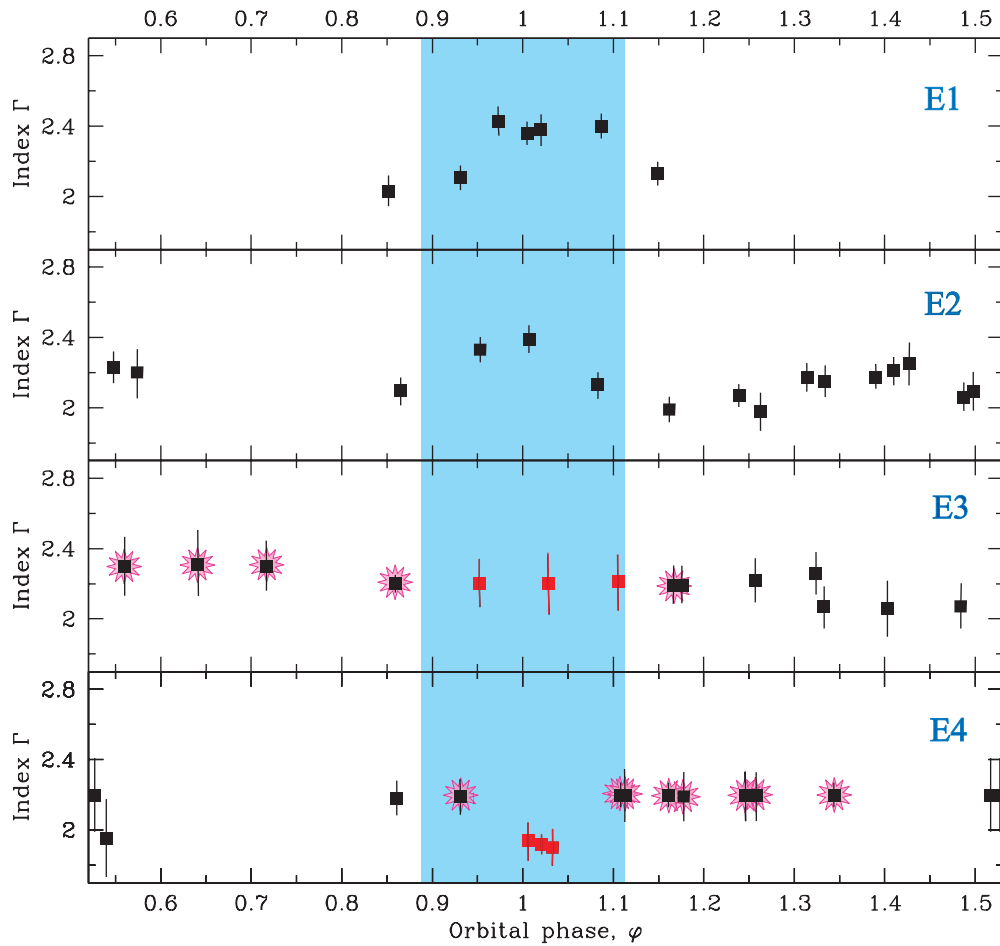


Figure 9. From top to bottom: photon index Γ vs. orbital phase φ during MJD = 50191–50194 (E1), 50897–50907 (E2), 52225–52238 (E3), and 53579–53588 (E4). The blue vertical strip marks an interval of the primary (optical) eclipse (Goranskij et al. 1998). Points marked with pink halos correspond to spectra fitted by the model which includes “high-temperature BB” component (see also Figure 1 and Tables 4–6). Red points (for two lower panels) correspond to observations during the primary eclipse when the “high-temperature BB” component is not detected, although it is present in spectral residuals before and after this eclipse. (A color version of this figure is available in the online journal.)

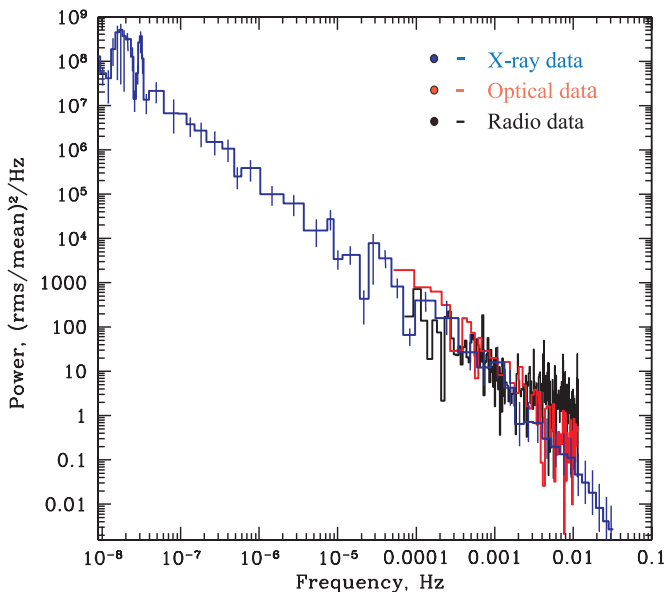


Figure 10. Power spectrum of SS 433 in three energy bands: X-ray (blue), 2.25 GHz radio (black), and V optical (red).

(A color version of this figure is available in the online journal.)

increases, to the spectra for which the power-law indices Γ stay almost the same and these Γ are always below 3 (see ST09 and Figure 8). In fact, the asymptotic values of Γ in SS 433 vary in the range ~ 2.2 – 2.3 (see Figure 8). Thus, we argue that the SS 433 X-ray observations reveal the index saturation versus mass accretion which can be a sign of a converging flow in this source indicating a BH presence. This index versus BMC normalization (proportional to the disk mass accretion rate) correlation can, in principle, allow us to estimate a lower limit of BH mass in SS 433.

To carry out the BH mass estimate in SS 433, we choose to scale the index–normalization previously found in GX 339–4 (see ST09) with that in SS 433 (see Figure 12). We can proceed with this scaling if these two correlations are self-similar. In other words, we implement this scaling technique when the given correlations have the same index saturation levels and slopes as a function of normalization (which is proportional to mass accretion rate in the disk).

Then, the value of the scaling coefficient provides us with the BH mass estimate. Note that the index–normalization correlation curve for the 2003 decay data of GX 339–4 (taken from ST09) is self-similar with that we find for SS 433.

Use of the scaling method for these two correlations provides the scaling coefficient $S_N = 14.9 \pm 0.7$, which is a

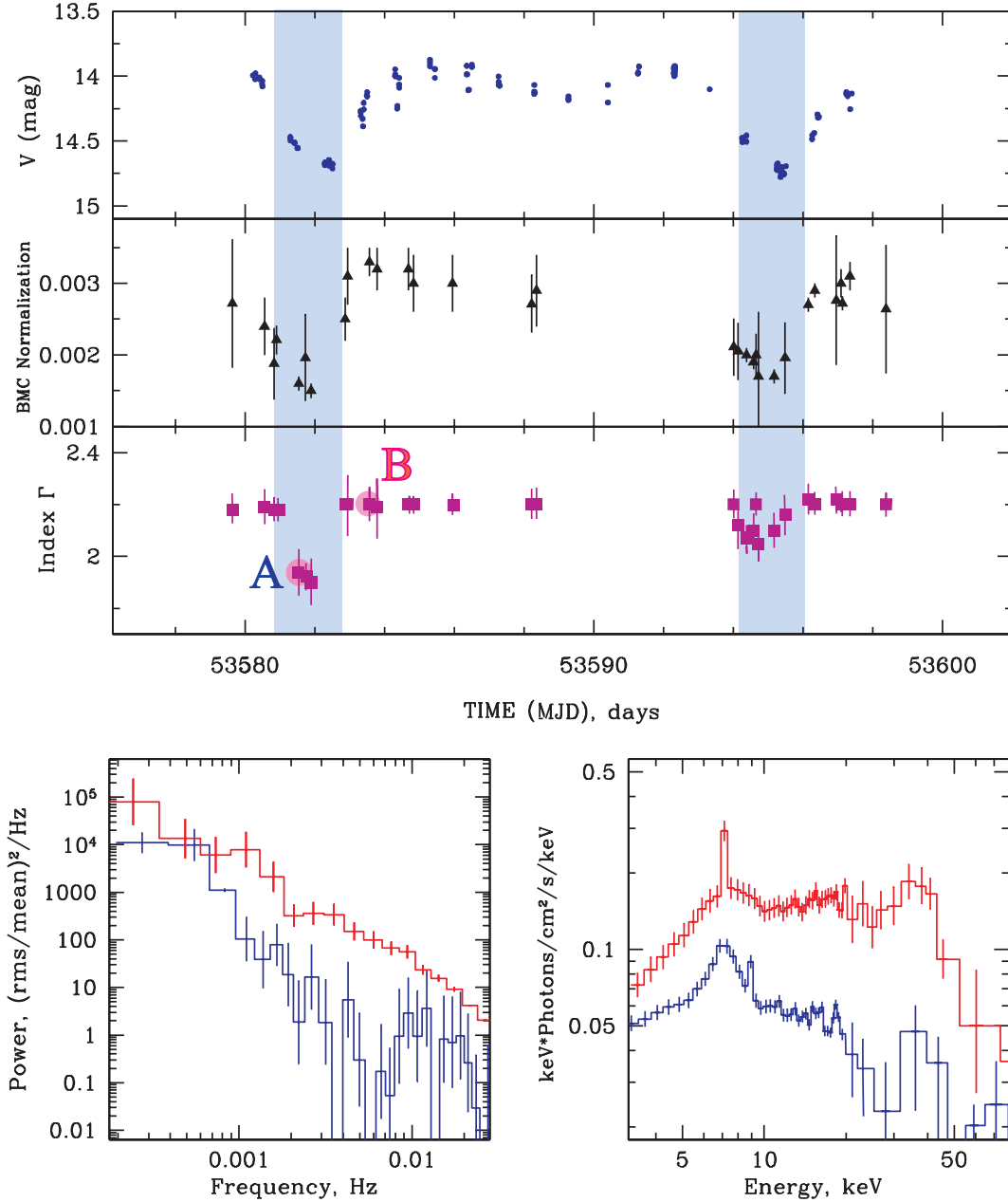


Figure 11. Top: from top to bottom: optical V-band light curve, BMC normalization, and photon index Γ for R6 set. Points A and B mark moments 53581 and 53585 (at eclipse and after eclipse), respectively. Blue strips mark eclipsed intervals of light curve. Bottom: PDSs (left panel) are plotted along with energy spectral diagram $E \times F(E)$ (right panel) for observational points A (1103-01-03-00, blue) and B (91103-01-07-00, red).

(A color version of this figure is available in the online journal.)

ratio (see ST09)

$$S_N = \frac{N_r}{N_t} = \frac{M_r d_t^2}{M_t d_r^2} f_G, \quad (2)$$

where M_r is the BH mass of the reference source (GX 339–4), M_t is the BH mass of the target source (SS 433), $f_G = (\cos \theta)_r / (\cos \theta)_t$ is the geometric factor, θ_r, θ_t are the inclination angles, and d_r, d_t are the distances to the reference and target sources, respectively. Here, the subscripts r and t are related to the reference and target sources, respectively. One can, in principle, estimate the BH mass M_t in SS 433 using relation (2). However, a value of the geometric factor $f_G = (\cos \theta)_r / (\cos \theta)_t$ is not obvious because $\cos \theta_r$, which is an inclination angle of the X-ray emission area in GX 339–4, is not known. Also, it

is not clear if we can use the inclination of the whole disk in order to estimate the inclination of the innermost part of the disk whose size is about 4 orders of magnitude less than that of the disk. This is one of the main problems in correctly evaluating f_G .

In order to estimate $(\cos \theta)_r = (\cos \theta)_{\text{GX}}$, we can apply the same formula (2) but using the target and reference sources GX 339–4 and GRO J1655–40, respectively. We take values of M_r, M_t, d_r, d_t , and $\cos \theta_{\text{GRO}}$ from ST09 (their Table 5) and then obtain the lowest limit of

$$(\cos \theta)_{\text{GX}} \gtrsim 0.4 \frac{(m_r/6.3)(d_t/5.75 \text{ kpc})^2 [(\cos \theta)_{\text{GRO}} / \cos 70^\circ]}{(m_t/12.3)(d_r/3.2 \text{ kpc})^2}. \quad (3)$$

Now we can resolve formula (2) with respect to $m_t = m_{\text{ss}}$ where we use GX 339–4 and SS 433 as the reference and target

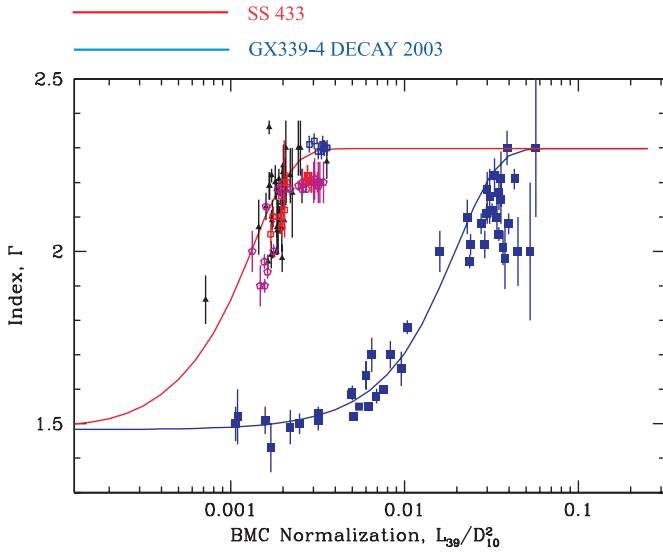


Figure 12. Scaling photon index vs. normalization for SS 433 (with red line—target source) and GX 339–4 (with blue line—reference source). (A color version of this figure is available in the online journal.)

sources, respectively. Thus, we obtain

$$m_{ss} \gtrsim 1.8 \frac{(D_t/5.0 \text{ kpc})^2 [(\cos \theta)_{GX}/0.4] (m_r/12.3)}{(D_r/5.75 \text{ kpc})^2 [(\cos \theta)_{ss}/0.17] (S_N/14.9)}, \quad (4)$$

where we use a value of $\cos \theta_{ss} \approx 0.17$ estimated by Cherepashchuk et al. (2005).

This is the lower limit mass estimate for SS 433 found using the ST09 scaling method. This estimate is consistent with the BH mass value $M_{ss} = (4.3 \pm 0.8) M_\odot$ obtained using optical observations of SS 433 (see Hillwig & Gies 2008, hereafter HG08). BH mass estimates for the reference (GX 339–4) and target (SS 433) sources are summarized in Table 7.

6.2. Upper Limit of the Size of “High-temperature BB-like” Bump Region

Now we try to estimate the upper limit of the size of the region Δl_{BB} from where the “high-temperature BB-like” photons originate. We consider the screening of the “BB-like” bump emitting region by the optical star with radius R_{st} .

Based on the BH mass estimate m_x by HG08, one can determine the mass of the donor (optical) star using the mass function of the normal star $f_v(m)$ for SS 433, namely,

$$f_v(m) = \frac{m_x^3 \sin^3 i}{(m_x + m_v)^2} = 1.038 \times 10^{-7} K_v^3 \times P_{orb} (1 - e^2)^{3/2}, \quad (5)$$

where $K_v = 58.2 \pm 3.1 \text{ km s}^{-1}$ is the semi-amplitude of radial velocity, $P_{orb} = 13.08$ days is the orbital period in days, e is the eccentricity ($e \sim 0$), and $i = 78^\circ 8'$ is the inclination angle of the system (see Margon 1984). Thus, the mass of the donor star m_v can be obtained as

$$m_v = \sqrt{\frac{m_x^3 \sin^3 i}{f_v(m)}} - m_x \simeq 12.3 M_\odot \quad (6)$$

if one resolves Equation (5) with respect to m_v and uses the BH mass values found by HG08 (see above). Then the resulting mass ratio is $q = m_x/m_v \leq 0.35$ (see HG08 and Filippova et al. 2006).

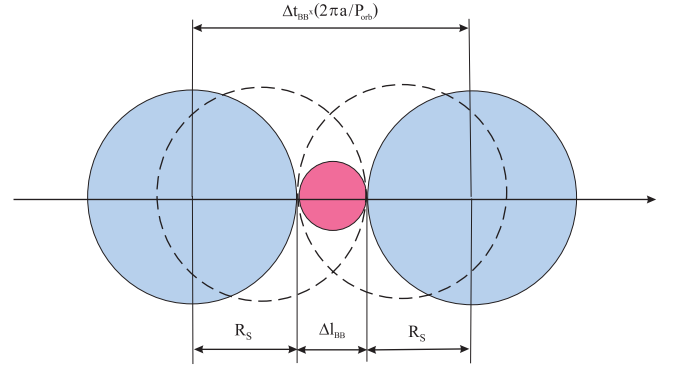


Figure 13. Eclipse of the inner X-ray emission region by optical star. (A color version of this figure is available in the online journal.)

Using the donor star mass, one can calculate the binary separation and Roche lobe radius. The resulting binary separation from Kepler’s third law is $a \sim 60 R_\odot$. Because the donor (optical) star in SS 433 fills its Roche lobe $R_{st} = R_{cr}$, the Roche lobe radius of the donor star can be found (compare with Eggleton 1983)

$$R_{st} \sim a \times \frac{0.49q^{-2/3}}{0.6q^{-2/3} + \ln(1 + q^{-1/3})} \sim 28 R_\odot. \quad (7)$$

But the upper limit of the “BB-like” bump-forming region can be estimated as

$$\Delta l_{BB} \sim \frac{2\pi a \Delta t_{BB}}{P_{orb}} - 2 \times R_{st} < 6.8 R_\odot, \quad (8)$$

assuming that the “BB-like” bump-forming region is screened, during $\Delta t_{BB} < 2.5$ days, by a donor (optical) star of radius R_{st} and rotating with the orbital velocity $v = 2\pi a/P_{orb}$ (see Figures 9 and 13). It is worth noting that Δl_{BB} , the real size of the “BB-like” component emission, should be significantly smaller than that we estimate by inequality (8). Here we have just found the upper limit of Δl_{BB} based on the direct observational estimates.

7. DISCUSSION AND SUMMARY

We derive a lower limit of 2 solar masses for the compact object in SS 4333 which clearly does not rule out a neutron star—this limit alone does not give strong observational evidence for a BH. This is the lower limit of the central object mass obtained using the sliding index–mass accretion correlation of SS 433 with respect to that for GX 339–4. In fact, this is an example where the sliding coefficient provides the lower limit of the mass of the central object. We remind the reader that this correlation of photon index and mass accretion rate was obtained using the so-called BMC model of XSPEC which is the first principle radiative transfer model. Namely, we consider and confirm applying the XSPEC fitting procedure that the emergent spectrum of the CC (the innermost part of a BH) is a result of upscattering of soft, presumably disk, photons off CC energetic electrons.

The crucial characteristic of the correlation is the saturation plateau which is a signature of the converging flow into the central object because the spectral index is an inverse of the Comptonization parameter Y which is a product of the number of scatterings, N_{sc} , and the average fractional energy change per scattering η (see also the details of the explanation of index saturation in Section 6.1). Only for converging flow, N_{sc} is

proportional to the optical depth τ of the cloud and η is inversely proportional to τ when τ is greater than 1. Thus, for large τ (mass accretion rate) it is natural to expect the index saturation as a signature of a BH and, in fact, we actually see this saturation in the case of SS 433. In other words, the main evidence for a BH is the index saturation with mass accretion rate. In contrast, in neutron star sources the photon index is almost constant, concentrating near 2, i.e., it does not change when mass accretion rate increases (see Farinelli & Titarchuk 2010).

Moreover, Hillwig & Gies (2008) found, using optical observations of SS 433, that the mass of the central object is 4.3 ± 0.8 solar masses which can be the case only for a BH. It is also worth noting a recent paper by Kubota et al. (2010) who argue that these mass values should be considered as upper limits, taking into account that the heating of the donor star may lower the derived masses to $1.9 M_{\odot} \leq M_X \leq 4.9 M_{\odot}$.

We find that the BMC model along with an additional “high-temperature bbody-like” component allow us to consistently describe the X-ray spectra of SS 433 and derive physical conditions during all states of SS 433. Moreover, our approach for data fitting demonstrates that the SS 433 spectra become softer, and finally the photon index saturates when the mass accretion rate increases during X-ray outburst. This index behavior is in agreement with ST09 and Titarchuk & Seifina (2009, hereafter TS09) previously found in a number of other BHC sources. Furthermore, the fits, using our spectral model, allow us to demonstrate that in some cases an additional “high-temperature bbody-like” component of color temperature of 4–5 keV appears in the data (see Figures 3–7 and Tables 4–6). This “bbody-like” feature arises only during the outburst transition of SS 433 and presumably originates in the innermost part of accretion flow (see discussion in Section 6.2).

Recently, we found a signature of this “high-temperature bbody-like” bump in *RXTE* spectral data for BHC GRS 1915+105 (see TS09). Also, we find that the same kind of “BB-like” bump is seen in *BeppoSAX* observations of the intermediate state of GRS 1915+105 (2000 April 21, ID = 209850011; Table 2). The data along with the model are presented in Figure 14 (top panel). Consequently, the presence of the additional “BB-like” bump spectral feature is not an instrumental effect of *RXTE* but can be a real observational feature of the observed spectra of BHCs. Furthermore, we also detected the same “bbody-like high-temperature” feature in the spectrum of SS 433 using the IBIS/ISGRI detector on board the *INTEGRAL* satellite during simultaneous observations with *RXTE* (ID = 90401-01-01-01, R5 set; see Figure 14, bottom panel). Thus, it is quite possible that this “high-temperature bbody-like” feature could be the universal signature of BH spectra.

One can also argue that the presence of the “high-temperature bbody-like” feature may be an artifact of having chosen the BMC model. In fact, the presence or absence of the bump can be related to the model. But the BMC model is a first principal Comptonization model and therefore any residual using this model can be considered as an observational signature of other components presented in the spectrum. Moreover, Laurent & Titarchuk (1999) and Laurent & Titarchuk (2010) demonstrate using a Monte Carlo simulation that X-ray emergent spectra of a BH for all spectral states are well fitted by the BMC model if the effect of pair production is not taken into account. But in the spectra of the intermediate and soft states, this additional “BB” feature appears if the nonlinear effect of pair creations in the very vicinity of a BH horizon is taken into account (P. Laurent & L. Titarchuk 2010, in preparation).

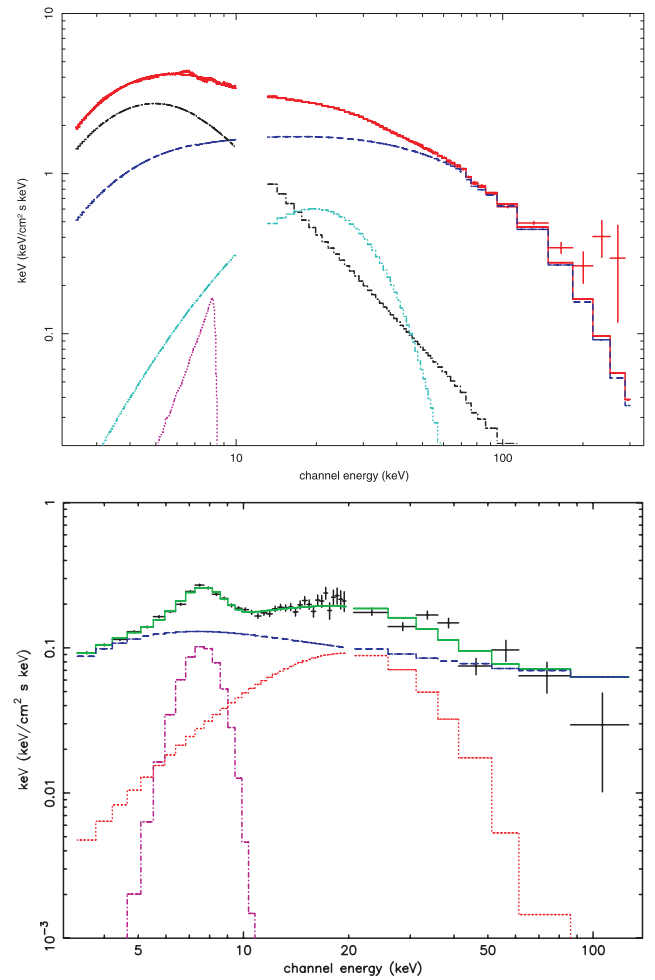


Figure 14. Broadband *BeppoSAX* spectrum of GRS 1915+105 (top) and *RXTE*/PCA and IBIS/ISGRI/*INTEGRAL* spectrum of SS 433 (bottom) in $E \times F(E)$ units obtained during the intermediate transition state of GRS 1915+105 on 2000 April 21 (ID = 209850011) and simultaneous *RXTE*/*INTEGRAL* observations of SS 433 for the outburst transition state on 2004 March 24–27.

(A color version of this figure is available in the online journal.)

One can say that such a bump seems very similar to the “Compton-bump” expected by reflection models in BH systems (both active galactic nuclei and stellar-mass objects), e.g., see Miller (2007). In fact, in our previous paper (TS09; see Section 4.2 there), we discuss this issue in detail. Here we should once again point out that in the observations this “high-temperature BB-like” bump appears only when the photon index is higher than 2. On the other hand, Laurent & Titarchuk (2007) demonstrate using a Monte Carlo simulation and theoretical arguments that the reflection bump never appears in the emergent spectra if the photon index of the spectrum Γ is higher than 2. Namely, there are not enough photons in the incident spectrum at high energies, if $\Gamma > 2$, to be re-emitted into lower energies due to scattering and recoil effects. In fact, as one can see from Tables 4–6 that in all spectra where we detect this “high-temperature BB-like” (~ 20 keV) feature index of the hard BMC component $\Gamma > 2$ and thus the appearance of this bump in the observed spectra cannot be explained by the so-called reflection effect.

TS09 argue that this “high-temperature BB-like” bump could be a result of the gravitationally redshifted annihilation line which is originally formed in the very vicinity of a BH horizon.

This feature (bump) should be seen in the IS and high soft state (HSS) spectra only because in these states the mass accretion rate is high enough to provide conditions to form the strong annihilation line and also to observe this feature through accreting material of relatively low plasma temperature (see more details in TS09, their Section 4.2).

It is worth noting that the time delay of the radio peak with respect to that in X-rays is two days for outburst rise (Revnivtsev et al. 2006). We find that during this X-ray flare, and then in the radio one, the object transits from IS to low hard state (LHS), which is quite unusual for spectral transitions of BHC. This particular behavior of SS 433 is different from other BH sources, probably because the jet is the dominant emission component. In general, when a BH goes to outburst it leaves a quiescent state, enters LHS, and then goes to an IS–HSS. However, the microquasar SS 433 is the only BHC which stays most of the time in IS with a rare short transition to LHS accompanied by the radio flare. A delay of the radio peak with respect to the X-ray peak is known during outburst rise transition in many X-ray BHC. However, the time delay value is different for each of the sources. For instance, it is about 20 days for GRS 1915+105 and about 2 days during outburst in SS 433. In the GRS 1915+105 case the index saturation value is about 3, whereas in the case of SS 433 the index saturates to $\Gamma \sim 2.3$. Moreover, the direct soft component, which is usually associated with the disk, is clearly seen in the GRS 1915 soft spectra and is weak or absent (at the level of detection) in most of the SS 433 spectra (see, e.g., Table 3).

As conclusions we formulate the following. We analyze the state transition data from SS 433 collected using *RXTE* observations. We examine the correlation between the photon index of the Comptonized spectral component and its normalization which is presumably proportional to the disk mass accretion rate (see Figure 8). We find that broadband energy spectra during all spectral states are well fitted by the XSPEC BMC model for the continuum and by two (broad and narrow) Gaussian line components. In addition to these model components, we also find a strong feature of a “BB-like” bump whose color temperature is in the range of 4–5 keV in 24 IS spectra of SS 433.

Furthermore, the application of our spectral model to the SS 433 data allows us to establish the saturation of the photon index versus BMC normalization, which scales with the disk mass accretion rate at value around 2.3 (see Figure 8). In addition, an application of the scaling method (see ST09) allows us to estimate a lower limit of compact object mass in SS 433 ($M_x > 1.8 M_\odot$).

A high value of the Comptonized emission fraction f obtained, in the framework of BMC model, gives us a strong evidence of significant reprocessing of the X-ray emission of the disk photons in SS 433 which is also in agreement with PDSs which reveal a pure power law (so-called red noise).

It is important to emphasize that the index saturation effect in SS 433 now seen is a BH signature and was recently found in a number of BHC sources (ST09). Moreover, the detection of the so-called high-temperature BB-like bump (which could be a gravitationally redshifted annihilation line) in SS 433 is also found in GRS 1915+105 data by different space missions (*RXTE*, *BeppoSAX*, and *INTEGRAL*).

We acknowledge Vitalij Goranskij and Tatyana Irmambetova who kindly provided us with optical data. We also thank the *RXTE* and *INTEGRAL* teams, and also Sergej Trushkin for providing us with X-ray and radio data, respectively. We

appreciated the comments and thorough editing of the paper made by Chris Shrader. We are very grateful to the referee for valuable comments and corrections of the content of the paper.

REFERENCES

- Antokhina, É. A., Seifina, E. V., & Cherepashchuk, A. M. 1992, *Sov. Astron.*, **36**, 143
- Band, W., et al. 1989, *ApJ*, **336**, 937
- Bradt, H. V., Rothschild, R. E., & Swank, J. H. 1993, *A&AS*, **97**, 355
- Brinkmann, W., Kawai, N., Matsuoka, M., & Fink, H. H. 1991, *A&A*, **241**, 112
- Brinkmann, W., Kotani, T., & Kawai, N. 2005, *A&A*, **431**, 575
- Cherepashchuk, A. M. 2002, *Space Sci. Rev.*, **102**, 1
- Cherepashchuk, A. M., et al. 2005, *A&A*, **437**, 561
- Cherepashchuk, A. M., et al. 2007, in Proc. VI INTEGRAL Workshop, The Obscured Universe, ed. S. Grebenev, R. Sunyaev, & C. Winkler (ESA SP-622; Noordwijk: ESA), **319**
- Churazov, E., Gilfanov, M., & Revnivtsev, M. 2001, *MNRAS*, **321**, 759
- Corvoisier, T. J.-L., et al. 2003, *A&A*, **411**, L53
- Eggleton, P. P. 1983, *ApJ*, **268**, 368
- Fabrika, S. N. 2004, *Astrophys. Space Phys. Rev.*, **12**, 1
- Farinelli, R., & Titarchuk, L. 2010, *A&A*, in press
- Fielder, S., et al. 1987, *ApJ*, **94**, 1244
- Filippova, E., Revnivtsev, M., Fabrika, S., Postnov, K., & Seifina, E. 2006, *A&A*, **460**, 125
- Gies, D. R., McSwain, M. V., Riddle, R. L., Wang, Z., Witta, P. J., & Wingert, D. W. 2002, *ApJ*, **566**, 1069
- Gilfanov, M., & Arefiev, V. 2005, arXiv:astro-ph/0501215
- Goranskij, V. P., et al. 1987, *Commun. Spec. Astrophys. Obs.*, **52**, 5
- Goranskij, V. P., et al. 1998, *Astron. Rep.*, **42**, 209
- Hillwig, T. C., & Gies, D. R. 2008, *ApJ*, **676**, L37
- Hynes, R. I., Steeghs, D., Casares, J., Charles, P. A., & O’Brien, K. 2004, *ApJ*, **609**, 317
- Kawai, N., Matsuoka, M., Pan, H., & Stewart, G. C. 1989, *PASJ*, **41**, 491
- Kotani, T., Band, D., Denisjuk, E. K., Kawai, N., Kinugasa, K., Namiki, M., Safi-Harb, S., & Trushkin, S. 2002, in ASP Conf. Ser. 279, *Exotic Stars as Challenges to Evolution*, ed. C. A. Tout & W. Van Hamme (San Francisco, CA: ASP), **19**
- Kotani, T., Kawai, N., Matsuoka, M., & Brinkmann, W. 1996, *PASJ*, **48**, 619
- Kotani, T., et al. 1994, **46**, L147
- Krivoshcheyev, Yu. M., Bisnovatyi-Kogan, G. S., Cherepashchuk, A. M., & Postnov, K. A. 2009, *MNRAS*, **394**, 1674
- Kubota, K., Kawai, N., Kotani, T., Ueda, Y., & Brinkmann, W. 2007, in ASP Conf. Ser. 362, *The Seventh Pacific Rim Conference on Stellar Astrophysics*, ed. Y. W. Kang et al. (San Francisco, CA: ASP), **121**
- Kubota, K., et al. 2010, *ApJ*, **709**, 1374
- Laurent, P., & Titarchuk, L. 1999, *ApJ*, **511**, 289
- Laurent, P., & Titarchuk, L. 2007, *ApJ*, **656**, 1056
- Laurent, P., & Titarchuk, L. 2010, *ApJ*, submitted
- Lopez, et al. 2006, *ApJ*, **650**, 338
- Lyubarskii, Yu. 1997, *MNRAS*, **292**, 679
- Margon, B. 1984, *ARA&A*, **22**, 5072
- Marshall, F. E., Swank, J. H., Boldt, E. A., Holt, S. S., & Serlemitsos, P. J. 1979, *ApJ*, **230**, L145
- Marshall, H. L., Canizares, C. R., & Schulz, N. S. 2002, *ApJ*, **564**, 941
- Matsuoka, M., Takano, S., & Makishima, K. 1986, *PASJ*, **38**, 285
- Miller, J. 2007, *ARA&A*, **45**, 441
- Munoz-Darias, T., Casares, J., & Martinez-Pais, I. G. 2008, *MNRAS*, **385**, 2205
- Namiki, M., Kawai, N., Kotani, T., & Makishima, K. 2003, *PASJ*, **55**, 281
- Nandi, A., Chakrabarti, S., Belloni, T., & Goldoni, P. 2005, *MNRAS*, **359**, 629
- Revnivtsev, M., et al. 2006, *A&A*, **447**, 545
- Romney, I. D., Schilizzi, R. T., Fejet, I., & Spencer, R. E. 1987, *ApJ*, **321**, 822
- Safi-Harb, S., & Kotani, T. 2003, in *New Views on Microquasars*, ed. P. Durouchoux, Y. Fuchs, & J. Rodriguez (Kolkata: Centre for Space Physics), **279**
- Seifina, E. 2000, *Astron. Rep.*, **43**, 305
- Shaposhnikov, N., & Titarchuk, L. 2009, *ApJ*, **699**, 453 (ST09)
- Sunyaev, R. A., & Titarchuk, L. 1980, *A&A*, **86**, 121
- Titarchuk, L., Lapidus, I. I., & Muslimov, A. 1998, *ApJ*, **499**, 315
- Titarchuk, L., Mastichiadis, A., & Kylafis, N. 1997, *ApJ*, **487**, 834
- Titarchuk, L., & Seifina, E. 2009, *ApJ*, **706**, 1463 (TS09)
- Titarchuk, L., Shaposhnikov, N., & Arefiev, V. 2007, *ApJ*, **660**, 556
- Titarchuk, L., & Zannias, T. 1998, *ApJ*, **499**, 315
- Watson, M. G., Stewart, G. C., King, A. R., & Brinkmann, W. 1986, *MNRAS*, **222**, 261
- Zwitter, T., Calvani, M., & D’Odorico, S. 1991, *A&A*, **251**, 92